Designing and Fabricating Color BRDFs with Differentiable Wave Optics

YIXIN ZENG, Zhejiang University, China
KISEOK CHOI, KAIST, South Korea
HADI AMATA, KAUST, Saudi Arabia
KAIZHANG KANG, Zhejiang University, China
WOLFGANG HEIDRICH, KAUST, Saudi Arabia
HONGZHI WU, Zhejiang University, China
MIN H. KIM, KAIST, South Korea

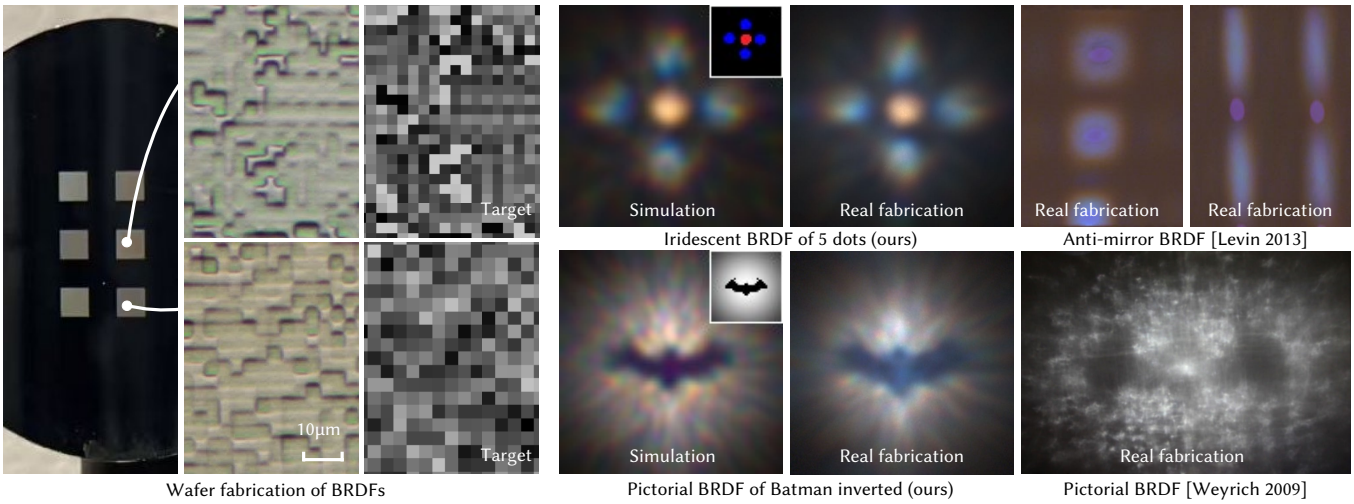

Fig. 1. Wafer fabrication of structural color BRDFs. The left three columns show microscopic and height map images of our fabricated wafer, produced using grayscale lithography at a feature resolution of 1.5–2.0 μm. The fourth and fifth columns present our BRDF simulation (with target insets) and corresponding real-world fabrication results, demonstrating angularly resolved reflectance with accurate control over both intensity and color. In the top row, we highlight our iridescent BRDFs–designed to exhibit structural color as a function of viewing direction. These results extend the prior work of the anti-mirror BRDFs by Levin et al. [2013], which offers no control over the color of the reflected light. In contrast, our method offers programmable angular and spectral control, producing multicolor effects not possible with prior work. In the bottom row, we demonstrate a pictorial BRDF (Batman inverted) fabricated using our method. Compared to Weyrich et al. [2009], whose geometric-optics-based method yields lower-frequency grayscale textures, our wave-optical formulation enables finer spatial resolution and additional color modulation through diffraction. The resulting reflectance pattern more faithfully captures the target image with enhanced visual contrast and directionality. To our knowledge, this is the first physically validated system capable of fabricating *color BRDFs* using wave optics, achieving both angular and spectral control over surface reflectance at micrometer-scale resolution. Refer to the supplemental video for more results.

Modeling surface reflectance is central to connecting optical theory with real-world rendering and fabrication. While analytic BRDFs remain standard in rendering, recent advances in geometric and wave optics have expanded the design space for complex reflectance effects. However, existing wave-optics-based methods are limited to controlling reflectance intensity only, lacking the ability to design full-spectrum, color-dependent BRDFs. In this work, we present the first method for designing and fabricating color BRDFs using a fully differentiable wave optics framework. Our differentiable and memory-efficient simulation framework supports end-to-end optimization of microstructured surfaces under scalar diffraction theory, enabling joint control over both angular intensity and spectral color of reflectance. We leverage grayscale lithography with a feature size of 1.5–2.0 μm to fabricate 15 BRDFs spanning four representative categories: anti-mirrors, pictorial reflections, structural colors, and iridescences. Compared to prior work, our approach achieves significantly higher fidelity and broader design flexibility, producing physically accurate and visually compelling results. By providing a practical and extensible solution for full-color BRDF design and fabrication, our method opens up new opportunities in structural coloration, product design, security printing, and advanced manufacturing.

Authors' Contact Information: Yixin Zeng, Zhejiang University, Hangzhou, China, 22221238@zju.edu.cn; Kiseok Choi, KAIST, Daejeon, South Korea, kschoi@vclab.kaist.ac.kr; Hadi Amata, KAUST, Thuwal, Saudi Arabia, hadi.amata@kaust.edu.sa; Kaizhang Kang, Zhejiang University, Hangzhou, China, cocoa_kang@zju.edu.cn; Wolfgang Heidrich, KAUST, Thuwal, Saudi Arabia, wolfgang.heidrich@kaust.edu.sa; Hongzhi Wu, Zhejiang University, Hangzhou, China, hongzhi.wu@gmail.com; Min H. Kim, KAIST, Daejeon, South Korea, minhkim@kaist.ac.kr.

ACM 1557-7368/2025/12-ART240
https://doi.org/10.1145/3763275

CCS Concepts: • **Computing methodologies** → **Reflectance modeling**; **Image-based rendering**.

Additional Key Words and Phrases: BRDF design, BRDF fabrication, reflectance modeling, structural color, wave optics

ACM Reference Format:
Yixin Zeng, Kiseok Choi, Hadi Amata, Kaizhang Kang, Wolfgang Heidrich, Hongzhi Wu, and Min H. Kim. 2025. Designing and Fabricating Color BRDFs with Differentiable Wave Optics. *ACM Trans. Graph.* 44, 6, Article 240 (December 2025), 17 pages. https://doi.org/10.1145/3763275

1 INTRODUCTION

Modeling surface reflectance is a fundamental topic in computer graphics. While simple analytic models remain widely used due to their efficiency and ease of use, more physically accurate approaches—based on microstructured surfaces—have been developed to capture complex reflectance behaviors. These models leverage geometric [Ashikmin et al. 2000; Cook and Torrance 1982] and wave optics [Stam 1999; Yu et al. 2023] to more accurately simulate light–surface interactions.

This advancement opens up new opportunities for applications such as structural coloration, product design, and high-resolution 3D printing, particularly when paired with the ability to fabricate surfaces with custom-designed reflectance properties.

Fabricating surfaces with controlled reflectance has broad practical value across domains such as 3D printing [Luongo et al. 2020], product design [Chermain et al. 2023; Weyrich et al. 2009], and security applications involving illumination-specific markers [Zyla et al. 2022]. Beyond visual appearance, customized bidirectional reflectance distribution functions (BRDFs) also play an important role in tasks such as microgeometry reconstruction [Johnson et al. 2011], appearance acquisition [Ren et al. 2011], and illumination measurement [Alldrin and Kriegman 2006]. These applications highlight the need for techniques that enable precise, programmable control over surface reflectance properties.

Recent advances have introduced several methods for fabricating surfaces with customized BRDF intensity distributions. Many of these approaches are grounded in geometric optics [Chermain et al. 2023; Hullin et al. 2011; Luongo et al. 2020; Weyrich et al. 2009; Wu et al. 2011], enabling the reproduction of diffuse or anisotropic specular lobes. Other techniques incorporate wave optics to achieve more complex reflectance behaviors [Levin et al. 2013; Pereira et al. 2017]. Despite these advances, existing methods remain limited in expressiveness, typically producing only simple anisotropic lobes or a small set of hand-crafted BRDF families. Moreover, all prior work focuses solely on shaping the intensity of reflected light. The ability to control the color of BRDF lobes remains entirely unaddressed.

Structural colorization has emerged as a compelling alternative to traditional pigment-based coloration, offering advantages such as vibrant appearance, long-term durability, environmental sustainability, and low energy usage. Unlike pigments, which selectively absorb parts of the visible spectrum, structural colors arise from the interaction of light with microscale surface features, producing phenomena such as iridescence. Recent methods have demonstrated the fabrication of structurally colored surfaces [Auzinger et al. 2018; Hwang et al. 2021; Zyla et al. 2022], but these approaches focus solely on diffuse color appearance and do not provide control over the angular intensity distribution of BRDF lobes.

In summary, previous approaches have enabled the fabrication of either BRDF intensities or structural colors, but not both simultaneously. However, joint control over angular and spectral reflectance is essential for applications where appearance must vary predictably with both direction and color. This includes tasks such as encoding view-dependent color shifts for anti-counterfeiting, engineering materials for spectrum- and angle-sensitive imaging systems, and designing responsive surfaces that adapt to illumination or viewing conditions. For example, a surface might reflect a red icon from one angle and a blue icon from another–an effect that cannot be achieved with pigments or angle-invariant structural coloration alone. This paper addresses this gap by introducing the first method to design and fabricate BRDFs with simultaneous control over both angular intensity and spectral color. We build upon recent wave-optics simulation techniques and develop a *differentiable wave optics pipeline* tailored for planar, high-reflectance surfaces. Our framework supports end-to-end optimization of surface microgeometry, enabling the physical realization of BRDFs with programmable spatial, spectral, and angular behavior.

To demonstrate the effectiveness of our approach, we fabricated a diverse set of fifteen BRDFs spanning four distinct reflectance profiles: anti-mirrors, pictorial reflections, structural colors, and iridescences. Fabrication was performed using grayscale lithography with a minimum controllable geometrical size (referred to as the feature size) of 1.5–2.0 μm, corresponding to 12,700–16,933 dpi, as shown in Figure 1. Our results show significant improvements over prior methods in both quality and generalizability, particularly in achieving joint control over directional reflectance and spectral color. By leveraging high-resolution fabrication and fully differentiable optimization, our method establishes a practical and extensible pipeline for manufacturing a wide range of customized BRDFs.

The key contributions of this work are:

- A fully differentiable wave-optics simulation framework that enables end-to-end optimization of surface microgeometry for both intensity and color control of BRDFs,
- A fabrication-aware formulation using a Gabor-kernel decomposition that incorporates spatial coherence, spectral sampling, and physical blur models to bridge simulation and real-world fabrication, and
- Demonstration of programmable BRDF families, including anti-mirror, pictorial, structural color, and iridescent reflectance patterns, fabricated on a wafer using grayscale lithography.

We anticipate that this framework opens new possibilities for BRDF-based encoding, structural coloration, and surface design in advanced optical fabrication. Our code and data are publicly available at https://github.com/KAIST-VCLAB/color-brdfs-with-wave-optics.

The rest of this paper is organized as follows. Section 2 reviews related work. Section 3 introduces the wave-optics preliminaries and presents our differentiable reflectance model. Section 4 describes the optimization framework. Section 5 covers the fabrication process and measurement setup. Section 6 presents experimental results and ablation studies. Section 7 discusses limitations and future directions, followed by conclusions in Section 8.

2 RELATED WORK

This section begins by examining current wave optics-based BRDF rendering methods tailored for explicit micro-surfaces, followed by

a discussion of our selected modeling approach. Additionally, we investigate material fabrication techniques that manage the light intensities and colors of the BRDF.

2.1 Wave-Optics Rendering

In geometric optics, BRDFs are defined as a pointwise mapping between differential solid angles of incident and outgoing directions, ignoring coherence and assuming locally defined interactions. However, wave optics models light as a complex-valued field that can exhibit interference and diffraction–effects that depend not only on direction but also on the *spatial coherence* of the light source.

Unlike geometric optics, which assumes perfectly incoherent light and sharp ray-path interactions, wave optics must consider how light waves combine coherently within a finite spatial region. The size of this region–known as the *coherence area*–is determined by the angular extent of the light source, shown in Figure 2.

We categorize wave-optics-based BRDF models based on the assumed extent of the illumination source–point-like or extended–and describe how each affects the coherence structure and rendering formulation.

Point light source. For a point light source, the incident field is spatially coherent across the entire surface, and reflected fields interfere globally. Early work assumed a far-field point light source. Under this assumption, Stam [1999] introduced a diffraction-based rendering model. The Harvey–Shack model [Harvey 1977] formulates diffraction using a surface transfer function, later adapted to graphics by Low et al. [2012] and Holzschuch and Pacanowski [2017]. These models offer high computational efficiency and are suitable for real-time rendering, but their idealized point lighting approximation limits their applicability in fabrication-oriented settings, where light sources have finite extent.

Extended light source. For extended light sources, coherence is limited to localized regions, and reflected fields interfere only within those regions. This distinction plays a central role in BRDF modeling under wave optics, as it defines how the surface modulates light and how reflected energy must be integrated across space. Subsequent methods model extended light sources to better approximate physical conditions. Dhillon et al. [2014] modified Stam's formulation using a spatial coherence window, enabling interactive rendering via precomputed Taylor series terms. However, these precomputations are not practical for differentiable pipelines due to the high cost of regeneration for each surface. Werner et al. [2017] extended wave-optical shading to scratched surfaces, while Yan et al. [2018] generalized this approach to arbitrary height fields using Gabor kernel decomposition for faster rendering. Falster et al. [2020] further expanded the framework to include multiple scattering via path tracing. Yu et al. [2023] presented a full-wave solver based on Maxwell's equations, offering the highest physical accuracy at the cost of extreme computational overhead. Balancing physical fidelity and computational efficiency, we adopt the Gabor-based model of Yan et al. [2018] as our forward rendering engine. We extend their method into a differentiable pipeline, enabling gradient-based optimization of microgeometry for BRDF design.

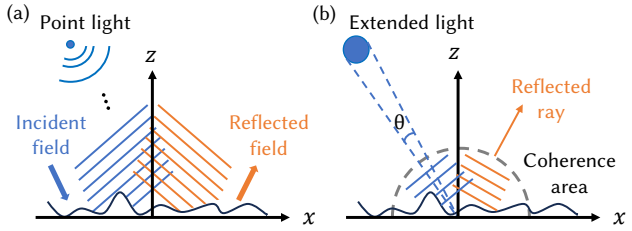

Fig. 2. Wave optics under different lighting conditions. (a) Under a far-field point light source, the incident illumination can be approximated as a planar wavefront over the microstructured surface. In this case, the reflected light field remains fully coherent and must be modeled using wave optics. (b) In contrast, real-world illumination typically originates from an extended light source, which subtends an angle θ on the surface. Coherent interference occurs only within a finite region known as the coherence area. Outside this region, wave interference diminishes, and the reflection behaves more like a ray, making geometric optics a suitable approximation.

2.2 Material Fabrication

Geometric optics-based. Fabrication methods based on geometric optics have been widely adopted in applications such as 3D object printing [Luongo et al. 2020; Piovarci et al. 2020], 2D reflectance control [Chermain et al. 2023], and dynamic BRDF displays [Hullin et al. 2011]. These approaches typically modify the surface at the macro- or meso-scale to produce simple BRDF features, such as diffuse or anisotropic specular lobes. Sakurai et al. [2023; 2018; 2023] demonstrate holographic paper fabrication, which corresponds to BRDFs with uniform intensity but angularly varying color. In contrast, Abu Rmaileh and Brunton [2023] achieve view-dependent color on 3D surfaces by embedding meso-scale facets and mapping their normals to color attributes. Weyrich et al. [2009] formulate a statistical microfacet distribution to match a target BRDF and fabricate the corresponding surface using precision milling. While their method can reproduce diverse BRDF shapes, its the geometric configuration limits the achievable spatial resolution, thus decreasing angular fidelity. Overall, geometric-optics-based fabrication methods either lack generality or suffer from insufficient resolution, which constrains their applicability to complex or color-varying reflectance.

Wave optics-based. Wave-optics-based fabrication methods offer higher spatial resolution and richer appearance effects. Pereira et al. [2017] use magnetic flakes to fabricate anisotropic reflectance, but their design is restricted to single-color effects and simple lobe shapes. Levin et al. [2013] employ wave optics to fabricate structured reflectance, such as anti-mirror BRDFs. However, their approach is hand-designed and limited to two BRDF families, without support for color variation. In contrast, our method enables the fabrication of BRDFs with jointly controlled intensity and color, using a fully differentiable wave optics simulation pipeline. We perform end-to-end optimization of surface microgeometry to match a target BRDF distribution, allowing us to generalize beyond fixed reflectance families or colors. This framework offers greater flexibility and expressive power than prior wave-optics-based approaches.

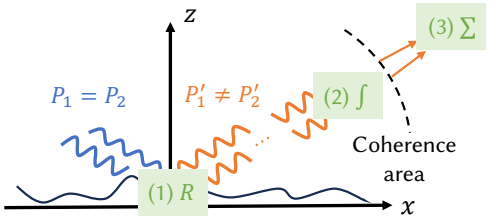

Fig. 3. Wave optics BRDF computation pipeline. (1) The surface induces a phase shift on the incident wave, captured by the complex modulation function R. The incident waves have identical phase ($P_1 = P_2$), while the reflected waves exhibit geometry-dependent phase shifts ($P_1' \neq P_2'$). (2) Within the coherence area, Kirchhoff integration is applied to coherently sum the reflected wave field. (3) Outside the coherence area, where spatial coherence is lost, the reflected intensity is computed by summing the squared magnitudes (i.e., incoherent energy addition).

2.3 Structural Coloration

Structural coloration techniques can be broadly categorized into three classes. Non-magnetic multilayer films generate color via thin-film interference [Chen et al. 2016; Chung et al. 2012], while metal-insulator-metal (MIM) structures rely on Fabry–Perot cavity resonances [Han et al. 2016; Wang et al. 2018]. These methods typically avoid complex nanofabrication steps but often result in strong angle-dependent color shifts. Photonic crystals, composed of periodic silicon-based nanostructures, can achieve angle-independent coloration [Cao et al. 2010; Shen et al. 2014], though their effectiveness is constrained by silicon's high optical absorption. More recently, plasmonic metasurfaces have enabled color generation based on surface plasmon resonances in metallic nanostructures [Franklin et al. 2015; Zhu et al. 2015]. For a comprehensive overview of artificial structural color mechanisms, see the review by Xuan et al. [2021].

Most of these methods address the forward problem of producing a color appearance from a fixed structure, without tackling the inverse design problem of customizing color through optimization. One exception is Auzinger et al. [2018], who use multiphoton lithography with transparent materials and optimize nanoscale structures via full-wave simulation to reproduce target colors. Hwang et al. [2021] explore color control using randomly distributed spherical microinclusions, optimizing parameters such as density, radius, and refractive index. Johansen et al. [2014; 2015] demonstrated control of surface color by optimizing nanoscale surface height under scalar diffraction theory. Andkjær et al.[2014] incorporated differentiable iridescent color generation into their pipeline, but to our knowledge, no fabricated results have been demonstrated.

In contrast, our approach supports both color and directional intensity control by simulating and fabricating BRDFs through a differentiable wave optics pipeline. We use a single metallic material and fabricate surfaces via a grayscale lithography process. This enables us to produce uniform colors within limited angular ranges, as well as iridescent effects and custom BRDFs with spatially varying intensity and color, offering a level of control beyond existing structural coloration methods.

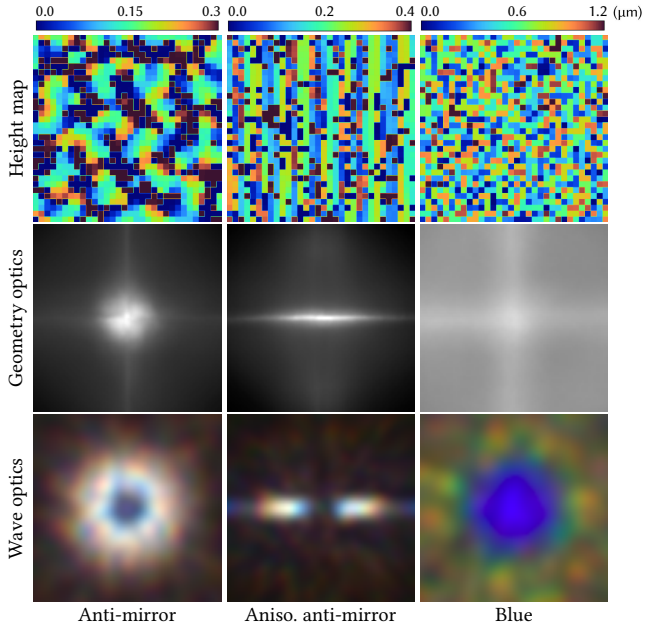

Fig. 4. Comparison of geometric optics and wave optics for three optimized BRDFs. We show rendering results for three BRDF designs–Anti-mirror, Anisotropic anti-mirror, and Blue reflectance–each optimized via our differentiable pipeline. For each case (left to right), the top row shows the corresponding optimized height map. The middle row shows renderings using geometric optics, while the bottom row shows results using wave optics. Geometric optics fails to capture anti-mirror effects or wavelength-dependent behavior, resulting in monochromatic and symmetric lobes. In contrast, wave optics accurately reproduces directional destructive interference of anti-mirror and spectral variations, including colored reflectance such as the blue lobe in the third column.

3 FORWARD BRDF MODELING IN WAVE OPTICS

3.1 Domain of Validity

Following the approach of Levin et al. [2013], we focus exclusively on surface reflectance and neglect effects due to refraction and material resonances. This implies our analysis concerns highly reflective materials with micron-scale features, since nano-scale features would give rise to resonance effects. For surface geometry, we model surface reflectance under the assumption that height variations are confined to the microscale. The surface is assumed to be globally planar, with its normal vector aligned to the positive z-axis, denoted by $\mathbf{n}$. Under this assumption, occlusion, shadowing, and masking effects are neglected.

For sufficiently distant light sources, the incident wavefront can be approximated as a plane wave (Figure 2(a)). Furthermore, when considering unpolarized illumination and reflection, the electromagnetic field can be modeled using a single complex-valued function under the scalar field assumption [Born and Wolf 1997], which neglects polarization and assumes time-harmonic wave behavior.

Under these approximations, classical models such as the Harvey-Shack model [Harvey 1977] and the Kirchhoff model [Beckmann and Spizzichino 1987] can be used to estimate the reflected wave field from microstructured surfaces. These models capture the inherently nonlinear nature of diffraction, where surface geometry modulates

both phase and amplitude, producing wavelength-dependent reflectance effects, including iridescent and colorful patterns, that cannot be explained by geometric optics alone (see Figure 4).

For a point light source, the reflected wave remains fully coherent across the surface and must be modeled using wave optics. However, real-world illumination typically originates from extended sources, which introduce partial spatial coherence (Figure 2(b)). As a result, interference effects are spatially localized within a finite region known as the *coherence area* [Goodman 1968], where the reflected wavefronts remain mutually coherent.

Within this coherence area, reflected light is represented as complex-valued fields and modulated by a surface-dependent complex reflection function. These fields interfere through coherent summation. Outside the coherence area, coherence is lost, and reflection is computed by aggregating intensity, i.e., summing the squared magnitudes of the individual fields, consistent with geometric optics. Although the far-field assumption is used across the paper, we found partial spatial coherence introduced by the coherence area is non-negligible, and an ablation about this is shown in Figure 10 in the Supplemental Document.

3.2 BRDF Formulation

Our BRDF formulation in wave optics follows the standard three-stage derivation introduced by Yan et al. [2018]. First, we compute the phase modulation induced by the surface geometry, encoded as a complex-valued modulation function R. Second, we integrate the reflected wave field within the coherence area; under the Kirchhoff approximation, this corresponds to taking the Fourier transform of R. Third, we square the magnitude of the complex field to obtain reflected intensity and combine it with incoherent contributions from outside the coherence area. These three steps are illustrated in Figure 3. Our method adopts this framework and accelerates the Fourier evaluation by decomposing R into a mixture of Gabor functions, enabling efficient and differentiable BRDF rendering.

Surface Geometry and Modulation. Following prior work [Levin et al. 2013; Stam 1999; Velinov et al. 2018], we represent surface microstructure using a height map $H(\mathbf{s})$, where $\mathbf{s} = [s_x, s_y]$ denotes a 2D position on the planar surface. An example of such a height map, along with one of our optimized results, is illustrated in Supplementary Figure 1 in the supplemental document.

Upon reflection, the surface height induces a phase shift in the wavefront, which depends on both the local height $H(\mathbf{s})$ and the incident wavelength λ. This effect is captured by a complex-valued modulation function $R(\mathbf{s})$, defined as:

$$R(\mathbf{s}) = \exp\left(-i\frac{2\pi}{\lambda}\xi_1 H(\mathbf{s})\right), \qquad \text{where } \xi_1 = \boldsymbol{\psi}\cdot\mathbf{n}. \tag{1}$$

Here, $\boldsymbol{\omega}_i$ and $\boldsymbol{\omega}_o$ denote the directions of the incident and reflected light, respectively, and $\boldsymbol{\psi} = \boldsymbol{\omega}_i + \boldsymbol{\omega}_o$. The surface normal $\mathbf{n}$ is assumed to be constant due to the globally planar surface assumption. The term ξ_1 accounts for the projection of the combined incident and reflected directions onto the surface normal and determines the phase gradient induced by height variations.

As discussed in Section 3.1, wave interference is spatially localized and occurs within a finite coherence area. We characterize the coherence area using a Gaussian kernel centered at a spatial point $\mathbf{x}_c$, corresponding to the center of coherence. The extent of coherence depends on the angular size of the light source, denoted by the subtended angle θ (in radians). The spatial weighting function is defined as:

$$w(\mathbf{s}-\mathbf{x}_c) = \frac{1}{2\pi\sigma_c^2}\exp\left(-\frac{\|\mathbf{s}-\mathbf{x}_c\|^2}{2\sigma_c^2}\right), \tag{2}$$

where $\sigma_c = \frac{\lambda}{6\theta}$ specifies the standard deviation of the Gaussian, and thus controls the coherence area size as a function of the wavelength λ and source angular spread θ. This kernel modulates the surface modulation function R, weighting each point's contribution based on its proximity to $\mathbf{x}_c$ in accordance with the spatial coherence decay.

Fourier Transform. Under the Kirchhoff approximation, the coherent component of surface reflectance can be expressed as the Fourier transform of the modulated surface function. Accordingly, the BRDF at a coherence center $\mathbf{x}_c$ is given by:

$$f_r(\boldsymbol{\omega}_i, \boldsymbol{\omega}_o; \lambda) = \frac{\xi_2}{A_c}\left|\int_{S_c} R^{\star}(\mathbf{s})\exp\left(-i\frac{2\pi}{\lambda}(\overline{\boldsymbol{\psi}}\cdot\mathbf{s})\right)d\mathbf{s}\right|^2, \tag{3}$$

where $\overline{\boldsymbol{\psi}}$ is the 2D projection of $\boldsymbol{\psi}$ obtained by discarding its z-component. The normalization factor $A_c = \int |w(\mathbf{s})|^2 d\mathbf{s}$. The term $R^{\star}(\mathbf{s}) = w(\mathbf{s}-\mathbf{x}_c)\,R(\mathbf{s})$ represents the surface modulation function weighted by the spatial coherence kernel. We adopt the reciprocal Original-Harvey-Shack (R-OHS) model [Yan et al. 2018] for angular dispersion, resulting in the prefactor:

$$\xi_2 = \frac{|\boldsymbol{\psi}\cdot\mathbf{n}|^2}{4\lambda^2\,|\boldsymbol{\omega}_\mathrm{i}\cdot\mathbf{n}|\,|\boldsymbol{\omega}_\mathrm{o}\cdot\mathbf{n}|}. \tag{4}$$

Coherence Area Integration. To enable efficient simulation of wave-based reflectance, we adopt the Gabor kernel formulation introduced by Yan et al. [2018]. A Gabor kernel $g(\mathbf{s})$ is defined as the product of a 2D Gaussian envelope and a complex-valued plane wave:

$$g(\mathbf{s};\boldsymbol{\mu},\sigma_g,\mathbf{a}) = G_{2D}(\mathbf{s};\boldsymbol{\mu},\sigma_g)\exp\left(-i2\pi(\mathbf{a}\cdot\mathbf{s})\right), \tag{5}$$

where $G_{2D}(\mathbf{s};\boldsymbol{\mu},\sigma_g)$ is a normalized isotropic Gaussian:

$$G_{2D}(\mathbf{s};\boldsymbol{\mu},\sigma_g) = \frac{1}{2\pi\sigma_g^2}\exp\left(-\frac{\|\mathbf{s}-\boldsymbol{\mu}\|^2}{2\sigma_g^2}\right). \tag{6}$$

In this formulation, $\boldsymbol{\mu}\in\mathbb{R}^2$ specifies the kernel center, σ_g controls the spatial extent of the Gaussian envelope, and $\mathbf{a}\in\mathbb{R}^2$ defines the spatial frequency vector of the oscillating complex component. This representation allows us to locally approximate the surface modulation function R using a linear combination of Gabor kernels, facilitating fast and differentiable Fourier evaluation.

We approximate the Fourier transform of R using a weighted mixture of Gabor kernels, rather than computing it directly. This formulation is not only computationally efficient but also well-suited for parallel processing. The resulting BRDF can be expressed as:

$$f_r(\boldsymbol{\omega}_i, \boldsymbol{\omega}_o; \lambda) = \frac{\xi_1}{A_c}\left|\mathcal{F}\left[R^{\star}\right]\left(\frac{\bar{\boldsymbol{\psi}}}{\lambda}\right)\right|^2 \tag{7}$$

$$\approx \frac{\xi_1}{A_c}\left|\sum_k w_k C_k \mathcal{F}\left[g\left(\mathbf{s};\mathbf{m}_k,\sigma_{g,k},\mathbf{a}_k\right)\right]\left(\frac{\bar{\boldsymbol{\psi}}}{\lambda}\right)\right|^2, \tag{8}$$

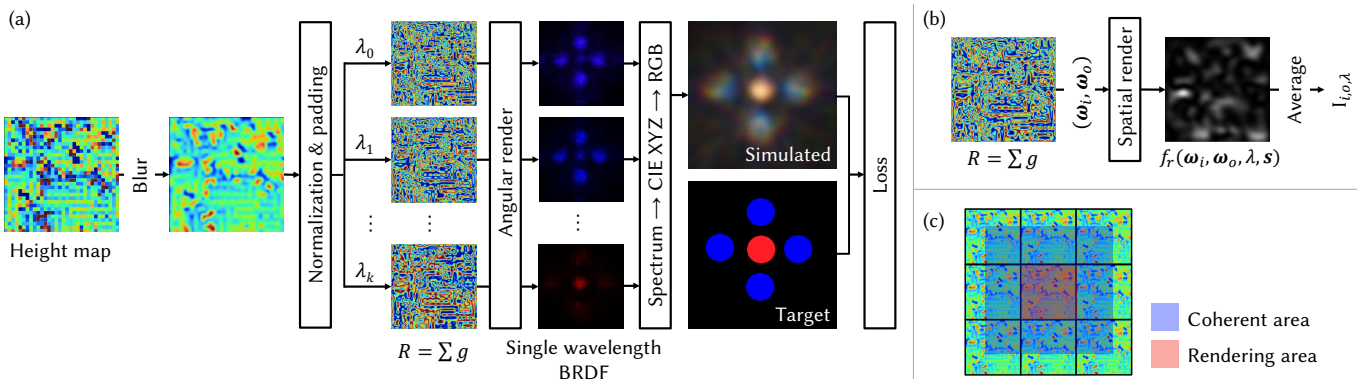

Fig. 5. Overview of our reflectance optimization framework. (a) Given a trainable height map, we first apply Gaussian blurring, followed by normalization and padding to enlarge the spatial domain for coherence-aware evaluation. For each sampled wavelength λ_k, the corresponding complex-valued surface modulation function $R = \sum g$ is constructed as a Gabor kernel mixture. BRDFs are rendered at each wavelength and then converted from spectral intensity to RGB via CIE XYZ transformation. The simulated RGB BRDF is compared with the target pattern to compute the loss. (b) Angular rendering pipeline. For each incident–outgoing direction pair (ω_i, ω_o), spatially resolved BRDF samples $f_r(\omega_i, \omega_o, \lambda, s)$ are computed within the center region. These are averaged to obtain the directional-spectral reflectance intensity $I_{i,o,\lambda}$, which serves as input to the final color synthesis and loss evaluation. (c) Illustration of padded height maps. The center patch (rendering area) is evaluated under coherence-aware reflection using surrounding padded tiles that account for spatial interference within each coherence area.

where $\mathcal{F}$ denotes the Fourier transform, and each term in the sum corresponds to a Gabor basis element centered at $\mathbf{m}_k$ with spatial scale $\sigma_{g,k}$ and frequency $\mathbf{a}_k$. The weight w_k modulates the contribution of the k-th component, while C_k is a complex-valued coefficient capturing amplitude and phase. For details on the derivation and computation of Gabor parameters from the height map H, we refer the reader to Yan et al. [2018].

Advantage of Gabor Decomposition. The Gabor decomposition used in our method provides several important advantages over traditional FFT-based wave propagation techniques. While FFT offers a global solution, it requires high-resolution simulations across all wavelengths and the entire spatial domain, resulting in significant memory overhead and limited scalability for iterative optimization. In contrast, Gabor functions have closed-form Fourier transforms and inherently local support, allowing us to compute reflectance within each Gabor independently. This locality enables efficient, parallelized evaluation on the GPU using shared memory, eliminating the need for storing large global buffers or intermediate states typically required for automatic differentiation. By performing analytical Fourier transforms of the Gabor kernels directly–rather than relying on global FFTs–we significantly reduce memory usage, avoid redundant computation, and accelerate both the forward and backward passes. As shown in Table 1, this decomposition improves runtime performance and scalability, making large-scale BRDF optimization under wave optics not only tractable but also practical for real-world fabrication tasks.

Color. To simulate color appearance, we sample eight discrete wavelengths uniformly spaced between 420 nm and 680 nm across the visible spectrum. For each wavelength, the reflected intensity is computed independently by evaluating the Gabor kernel mixture in the Fourier domain. The resulting intensity is then scaled by the wavelength-dependent Fresnel coefficient of the surface material. We assume a uniform illumination spectrum, i.e., equal energy distribution across all sampled wavelengths. The spectral intensities are converted to RGB values through a standard spectrum-to-CIEXYZ-to-sRGB transformation. To evaluate and optimize BRDF appearance at the spatial level, we average the reflected intensities over a small neighborhood of features. Following Levin et al. [2013], we define this neighborhood size based on the projected surface area corresponding to a single pixel at the target display resolution, also referred to as the *patch* size.

4 BACKWARD BRDF OPTIMIZATION IN WAVE OPTICS

We now address the inverse problem in designing a surface microstructure that produces a target BRDF. This requires computing gradients of wave-optical reflectance with respect to surface geometry–a task complicated by the non-local and interference-driven nature of light propagation. Unlike geometric models, wave-optics-based BRDFs depend on phase interactions integrated over spatial coherence regions. To make this optimization tractable, we develop a fully differentiable wave-optics pipeline that enables end-to-end optimization via Fourier-based rendering, coherence modeling, and spectral integration.

4.1 Differentiability in Wave Optics

While gradient-based inverse design is well established in differentiable holography [Chen et al. 2023], near-eye holographic display [Chakravarthula et al. 2019], diffractive optical element (DOE) design [Jeon et al. 2019; Sitzmann et al. 2018], and diffractive optics [Baek et al. 2021; Peng et al. 2019; Sun et al. 2020], its application to BRDFs remains largely unexplored. In this work, we bring differentiable wave-optical modeling into the BRDF space, enabling surface geometry to be optimized directly for both angular and spectral reflectance.

In addition, we formulate this optimization using *scalar diffraction theory*, which provides a tractable approximation of wave propagation while exposing closed-form derivatives for phase and amplitude. To efficiently support gradient computation across coherence regions, we introduce a *Gabor kernel decomposition of the surface modulation function*, allowing fast, differentiable Fourier rendering. This formulation serves as the foundation for our end-to-end optimization pipeline and is key to producing spatially and spectrally programmable BRDFs at the micrometer scale:

- The optical field is represented as a complex-valued wavefront $E(\mathbf{x}) = A(\mathbf{x})e^{i\phi(\mathbf{x})}$, capturing both amplitude and phase explicitly.
- Surface-light interactions are modeled using the *reciprocal R-OHS* theory, which provides an analytic relationship between surface height and phase modulation via the surface reflection function R. Notably, the material affects only amplitude, not phase, simplifying the gradient path.
- Wave propagation is computed using *Kirchhoff integration*, which maps directly to a Fourier transform, allowing efficient and differentiable rendering in the frequency domain.

This formulation forms the core of our optimization framework, enabling direct gradient flow from rendered BRDFs back to surface geometry. Figure 5 provides an overview of our optimization framework. To our knowledge, this is the first differentiable wave-optics BRDF pipeline that jointly models interference, diffraction, and spectral color within a tractable optimization loop. However, the periodic nature of the phase with respect to optical path length can introduce high-frequency gradient oscillations, potentially leading to local minima during training. We address this with carefully designed training parameters and controlled sampling strategies, as described in later sections.

4.2 Memory-Efficient Backward Propagation

As illustrated in Figure 5, our goal is to optimize the surface height map H to match a target BRDF through a fast and differentiable wave optics simulation. While automatic differentiation frameworks such as PyTorch offer a convenient starting point, they are ill-suited for the structure of our problem. In particular, PyTorch requires tensors to be stored contiguously in memory and parallelizes operations over entire batches. However, our rendering pipeline involves computing BRDFs over localized coherence areas, which act as sliding windows across the height map (see Equation (8)).

To align with PyTorch's requirements, one would need to unfold the Gabor kernels into overlapping windows, duplicate data into contiguous memory blocks for each window, and then merge them into a large tensor for batch computation. This procedure introduces significant memory overhead and computational inefficiency–bottlenecks that become prohibitive in high-resolution, iterative optimization scenarios.

To overcome these limitations, we introduce a custom CUDA-based backward propagation framework tailored to the structure of spatially local, coherence-aware BRDF rendering. This approach avoids the costly data duplication required by generic autodiff systems, enabling a scalable and memory-efficient optimization process.

Table 1. Comparison of simulation speed and memory usage across wave-optics-based BRDF simulation methods. All methods are evaluated under identical settings using a 32×32 height map with a 4×4 sampling rate, consistent wavelength sampling, feature size, and coherence area. All experiments–except Yu et al. [2023], which requires at least four GPUs–are conducted on a single NVIDIA GeForce RTX 4090 GPU. For Yan et al. [2018], we include both the GPU and CPU implementations; the latter is run on a dual AMD EPYC 7763 server with 768 GB DDR4 memory. Our method achieves the fastest rendering time and the lowest memory footprint, demonstrating a 7× speedup and 30× memory reduction compared to the GPU version of Yan et al.

	[Yu 2023]	[Levin 2013]	[Yan 2018]	[Yan 2018]	Ours
Speed (hr)	819.2	2.6	16.0	9.6	1.3
Memory (GB)	0.59×4	10.7	–	16.1	0.49
Device	GPU	GPU	CPU	GPU	GPU

To overcome the inefficiencies of general-purpose autodiff frameworks, we design a custom CUDA-based solution inspired by recent GPU-accelerated Gaussian rendering methods [Kerbl et al. 2023; Wurster et al. 2024]. In our formulation, each query corresponds to a spatial sample that requires evaluation of the BRDF over its local coherence area. Rather than duplicating Gabor kernels across all windows, we record the indices of relevant Gabors for each query and fetch their parameters into fast shared memory *on-demand* during execution. This approach avoids unnecessary memory duplication and significantly improves computational throughput.

To enable parallel evaluation, we divide the Gabor field into blocks of 16×16 spatial samples, with each block processed by 512 CUDA threads. Within each thread, the BRDF is evaluated in the Fourier domain by aggregating contributions from all Gabors inside the coherence area centered at the query point.

A key distinction from traditional Gaussian or Gabor splatting is that, in our case, the reflectance of a sample depends on the neighboring samples within its coherence region–not just on its block. To account for this dependency, each CUDA block must access an extended region of size $(16 + N_c) \times (16 + N_c)$, where N_c is the coherence radius in one feature. As a result, the computation blocks overlap, with an overlap margin of N_c along each axis. This coherence-aware block tiling strategy is central to our GPU-efficient optimization pipeline, enabling us to scale BRDF rendering to dense spatial grids with high-frequency structure.

We derive gradients explicitly using the mathematical properties of Gabor kernels and the chain rule, thereby avoiding numerical differentiation. Although our approach does not involve solving an adjoint equation as in classical adjoint methods, it achieves comparable efficiency by leveraging analytical expressions for both forward and backward passes, fully exploiting GPU parallelism and memory bandwidth.

Because wave optics rendering is inherently compute- and memory-intensive, differentiability alone is not sufficient for practical optimization. Our CUDA-based pipeline achieves an order-of-magnitude improvement in both runtime and memory footprint: it is approximately 7× faster and consumes only 1/30 of the GPU memory compared to a baseline implementation of Gabor-based BRDF rendering. A detailed comparison of simulation speed and memory usage across several state-of-the-art methods is provided in Table 1.

Multiple Solutions. For single-wavelength BRDFs, it is possible to optimize BRDFs by adjusting the Gabor parameters, computing the surface modulation function R from the fitted Gabor decomposition, and then attempting to reconstruct a corresponding height map. Although this inverse mapping is generally not unique–since R is a periodic function of the surface height H (as shown in Equation (1))–it is still feasible to select one valid height field for fabrication in the single-wavelength case.

However, this approach becomes significantly more difficult in the multi-wavelength setting. Finding a single height field that simultaneously satisfies the modulation functions R across all wavelengths becomes a highly non-convex, mixed-integer problem. Moreover, to ensure manufacturability, additional physical constraints must be imposed on the geometry, making it impractical to stitch together per-wavelength solutions. This challenge fundamentally limits the extension of methods such as Levin et al. [2013], which rely on hand-designed sampling and cannot support wavelength coupling or color fabrication.

To avoid this complexity, we choose to directly optimize the height map itself. This formulation ensures wavelength compatibility and allows us to incorporate fabrication-specific constraints, such as bounded height ranges, minimum feature sizes, and physical smoothness, and enables seamless extension to more advanced fabrication-aware models, including differentiable lithography simulation. While this approach sacrifices global optimality in favor of tractability (yielding local minima), it significantly improves practicality and generalizability.

4.3 Sampling

Accurate sampling is essential for stable and high-fidelity optimization in our differentiable wave optics pipeline. While prior work in BRDF rendering via wave optics [Yan et al. 2018] reported that one Gabor kernel per feature was sufficient, their examples involved relatively low-frequency height maps. In contrast, our optimization process can generate high-frequency geometric detail, where insufficient sampling introduces aliasing and distortion.

To evaluate the effect of sampling resolution, we conduct an ablation study, summarized in Figure 6. We compare spatial and angular accuracy under four sampling densities: 1×1, 2×2, 4×4, and 8×8 Gabors per feature. The results show that 1×1 and 2×2 fail to preserve critical phase structures in the modulation function R, while 4×4 and 8×8 sampling achieve much higher fidelity. Based on this analysis, we use 4×4 sampling during optimization and 8×8 sampling for final rendering throughout the paper. This corresponds to 16 Gabors per feature, and angular BRDF rendering is performed using a patch of 128×128 queries. To further suppress aliasing, we apply a Gaussian blur with standard deviation $\sigma_b = 0.13\,\mu$m to the height map before computing R.

Second, during optimization, we address directional sampling for the incident and outgoing directions, $\boldsymbol{\omega}_i$ and $\boldsymbol{\omega}_o$. While we begin with uniform concentric disk sampling, we observe that optimized BRDFs often exhibit unwanted specular spikes near the mirror direction. As previously noted by Levin et al. [2013], these spikes result from low-frequency components in the height map that produce

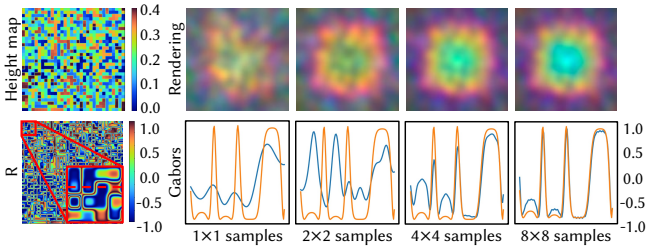

Fig. 6. Effect of sampling rate on BRDF rendering accuracy. Left: input height map (top) and the corresponding complex modulation function R (bottom), derived from reciprocal R-OHS theory. The inset indicates the horizontal line used for the 1D slice comparison. Right: BRDF rendering and 1D approximation results for four sampling rates (1×1 to 8×8). Top: rendered BRDFs. Bottom: real part of the Gabor approximation (blue) versus ground truth R slice (orange). Based on this analysis, we use 4×4 sampling for optimization and 8×8 for final rendering throughout the paper. The unit used in both the colorbar and the line chart is μm.

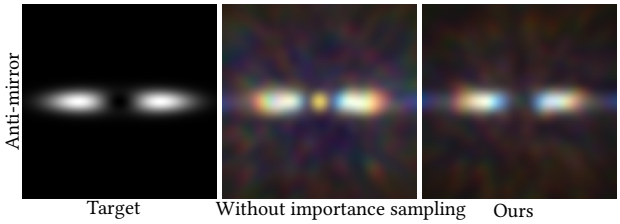

Fig. 7. Impact of importance sampling on angular BRDF fidelity. We compare rendering results for a high-frequency Anisotropic Anti-mirror target (left) optimized using uniform sampling (center) and our importance sampling strategy (right). Without importance sampling, the BRDF exhibits a strong, unwanted specular spike in the center due to Fourier-domain impulses. Our method reduces this artifact and more accurately reproduces the desired angular profile.

impulses in the Fourier domain. Such components are difficult to suppress, especially under spatial resolution constraints.

To mitigate this artifact, we introduce an *importance sampling strategy* by squaring the normalized direction vectors, which concentrates samples near the center of the angular domain. This reallocation encourages the optimization to more effectively suppress the central specular spike. As shown in Figure 7, our method achieves noticeably improved angular contrast and suppression of the undesired central lobe, compared to uniform sampling.

4.4 Optimization

We optimize the BRDF by minimizing the difference between the rendered and target reflectance under full-spectrum illumination. Our rendering pipeline evaluates eight discrete wavelengths and converts the spectral reflectance to sRGB using a standard CIEXYZ-based transformation [Fichet et al. 2021]. For each angular pair $(\boldsymbol{\omega}_i, \boldsymbol{\omega}_o)$, the predicted BRDF is spatially evaluated and averaged over a *patch area*. We use a default patch size of 32×32 features throughout our implementation, while maintaining flexibility for user-specified dimensions (see Supplementary Figure 8 for ablation). This parameter physically corresponds to the surface area of a single pixel when projected at the target display's resolution.

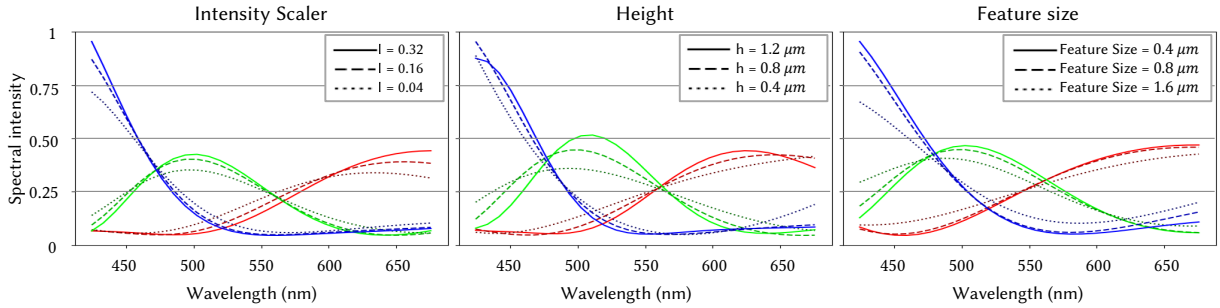

Fig. 8. Spectral intensity curves of Red, Green, and Blue BRDFs under varying training parameters. We render reflectance profiles at the center of the BRDF lobe (20°) using 30 wavelength samples between 420 nm and 680 nm, and plot the spectral response for each color. Three ablation studies are shown: (left) intensity scaling factor, (middle) maximum height range h, and (right) feature size. Sharper spectral peaks are observed with increased height, larger intensity scaling, or finer feature size, leading to stronger color selectivity. For RGB renderings corresponding to these spectra, refer to Supplementary Figure 9 in the Supplemental Document.

Let $f_r(\boldsymbol{\omega}_i, \boldsymbol{\omega}_o, \mathbf{s})$ denote the BRDF in sRGB at spatial sample $\mathbf{s}$, and let $I_{i,o} = \frac{1}{N}\sum_s f_r(\boldsymbol{\omega}_i, \boldsymbol{\omega}_o, \mathbf{s})$ be the spatially averaged reflectance intensity over N samples within the patch area. Let $\bar{I}_{i,o}$ denote the corresponding ground truth BRDF under the same angular configuration. We define a simple photometric loss in RGB space as:

$$\mathcal{L} = \sum_m (I_m - \bar{I}_m)^2. \tag{9}$$

where I_m and $\bar{I}_m$ denote predicted and ground truth RGB values across all angular samples m. We refer to the per-sample evaluation as *spatial rendering* and the final patch-wise averaging as *angular rendering*, as illustrated in Figure 5(b).

Our optimization directly operates in height space–without relying on regularization or hand-crafted priors. In contrast to Levin et al. [2013], who predefine discrete BRDF families and apply heuristic algorithm, our method jointly optimizes reflectance across the full visible spectrum via a fully differentiable simulation pipeline. This approach offers two key advantages: First, it enables precise control over both intensity and color distributions across angles and wavelengths. Second, it supports arbitrary BRDF patterns, including complex and color-structured reflectance profiles, while respecting physical and fabrication constraints.

5 REAL FABRICATION

5.1 Consideration for Real Fabrication

To bridge the gap between simulation and real-world fabrication, several practical factors must be addressed: patch padding for coherence overlap, BRDF scale ambiguity, and fabrication-aware height map constraints. To be specific, we pad the central patch with replicated height data, as illustrated in Figure 5(c). We control the reflection intensity with an intensity scaler, and constrain the height map to a fixed range $[0, h]$ during optimization. Furthermore, to model noise during fabrication, we apply a Gaussian filter with a standard deviation of σ_b to the height map and incorporate relative Gaussian noise with a standard deviation of σ_n. For more detailed discussion, please refer to Section C in the Supplemental Document.

Based on these designs, we investigate how intensity scaler, height range, and feature size influence the color quality, shown in Figure 8. Excessive scaling amplifies noise and distorts the relative energy distribution across wavelengths, while insufficient scaling underemphasizes high-frequency reflectance features. We carefully choose the proper scaler for every BRDF tested. Larger height ranges and smaller feature sizes lead to better color quality, but also increase fabrication difficulty. We choose a maximum height of 0.8 μm and a feature size of 1.6 or 2 μm for real-fabrication based on this understanding. These studies inform the fabrication-aware constraints used throughout our pipeline, ensuring both physical viability and high-fidelity rendering.

5.2 Grayscale Lithography

Grayscale lithography is a versatile fabrication technique widely used for creating 3D micro- and nanoscale surface structures. It has been applied in domains such as biostructure engineering [Fallica et al. 2017; Mühlberger et al. 2015], microlens fabrication [Aristizabal et al. 2013; Deng et al. 2017], and structural color generation [Chen et al. 2022]. Compared to traditional binary mask-based photolithography, as employed in Levin et al. [2013], grayscale lithography provides several advantages that make it especially well-suited for fabricating customized BRDFs.

Conventional lithographic processes rely on hard masks with strictly binary transparency (opaque or transparent). Fabricating multi-level structures with such methods requires multiple exposures using precisely aligned masks. However, maintaining accurate alignment is challenging, and even small registration errors–typically on the order of hundreds of nanometers–can significantly distort the fabricated geometry, as reported in prior work [Jeon et al. 2019; Peng et al. 2016; Shi et al. 2024; Sun et al. 2020].

In contrast to binary photolithography, grayscale lithography enables continuous surface reliefs by modulating exposure intensity across the substrate. This can be achieved in two main ways: (a) using spatial light modulators such as digital micromirror devices (DMDs) or liquid crystal displays (LCDs) to project intensity-modulated patterns; or (b) using direct laser writing, in which a focused laser beam scans the surface and the local exposure is controlled by dynamically adjusting the beam's intensity. In both cases, the process allows for maskless, single-step exposure based on grayscale input images. Our fabrication system uses the direct laser writing approach. This method offers high spatial resolution

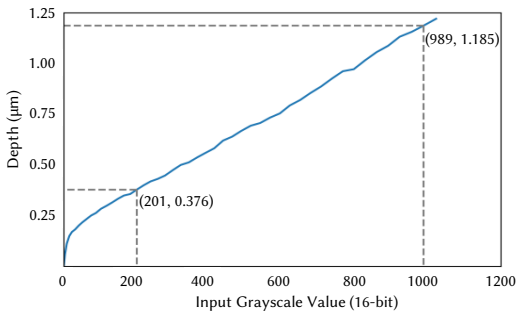

Fig. 9. Depth calibration curve for grayscale lithography. We empirically determine the mapping between 16-bit input grayscale values and fabricated depth in photoresist. To ensure accuracy in reproducing surface geometry, simulation heights are scaled to a calibrated range of $[0.376, 1.185]\,\mu$m, corresponding to input values between 201 and 989.

Fig. 10. Ablation study of different coating materials on simulated BRDF appearance. We conduct optimization towards the same target using the Fresnel coefficients of five materials: Ag, Al, Cr, Cu, and Si. Materials with broad, uniform reflectance (Ag, Al, Cr) preserve color and angular structure, while spectrally selective metals like copper produce distorted or muted results. These simulations guide the selection of aluminum as the preferred coating for physical fabrication.

and precise depth modulation, making it well suited for fabricating microstructured surfaces where accurate phase control is critical. Compared to conventional multi-mask lithography, grayscale lithography avoids inter-layer misalignment and achieves superior z-axis resolution–key advantages for producing BRDFs with angle- and color-sensitive microgeometry.

Although binary lithography can achieve finer lateral resolution, grayscale lithography is more suitable for our application due to its ability to produce smooth, multi-level height fields in a single pass. In our BRDF fabrication pipeline, even minor misalignments or quantization errors can severely affect angular reflectance. For this reason, we adopt grayscale lithography as our fabrication method.

Depth calibration. To ensure precise correspondence between simulated height values and fabricated geometry, we perform a calibration process that maps grayscale pixel values to physical depth. Using test exposures, we empirically establish a nonlinear response curve between 16-bit grayscale input values and resulting etched depths in photoresist. As shown in Figure 9, we map the height field to a calibrated depth range of $[0.376, 1.185]\,\mu$m, corresponding to pixel values in the range $[201, 989]$. This mapping is used to convert our simulated height maps into 16-bit grayscale images that are fed to the lithography system. This calibration is essential for accurate reproduction of microstructure geometry in the final BRDF fabrication.

Alternative methods. While two-photon lithography [Auzinger et al. 2018] offers extremely high resolution (below 200 nm in both lateral and depth directions), it suffers from several practical drawbacks. These include high equipment cost, resist shrinkage, and very low throughput [Grushina 2019], which limit its scalability. For these reasons, we do not pursue this technique here, but consider it a promising direction for future exploration.

5.3 Real Fabrication

Fabrication. We fabricated our prototypes using the grayscale lithography mode of the Heidelberg DWL66+ laser writer, equipped with a 5 mm write head. This system allows precise laser intensity modulation to encode continuous 3D surface profiles in photoresist directly. Each BRDF design is patterned onto AZ 4562 photoresist by spatially varying the laser dose, achieving a single-step exposure without masks.

To ensure accurate reproduction of surface geometry, we use the pre-calibrated grayscale-to-depth mapping described in Figure 9. Our pipeline converts the optimized height maps into 16-bit grayscale images that match the calibrated fabrication range. Following development, a 50 nm aluminum layer is deposited using an ESC Ion Beam Assist Sputter system (model ESCRD4), providing a high-reflectance metallic surface. This fabrication process enables direct realization of simulation-optimized BRDFs onto wafer-scale surfaces. For each BRDF example, we fabricate a 50 mm × 50 mm square on the wafer for reflectance measurement.

We evaluate the impact of different metal coatings on the final BRDF appearance by conducting optimization towards the same target using the Fresnel coefficients of five candidate materials: silver (Ag), aluminum (Al), chromium (Cr), copper (Cu), and silicon (Si). As shown in Figure 10, most materials with strong and relatively flat reflectance spectra (e.g., Ag, Al, Cr) reproduce the designed BRDF shape and color faithfully. In contrast, copper, which exhibits significant spectral non-uniformity, introduces color shifts and reduces angular fidelity. Based on these results, along with considerations of cost, availability, and compatibility with our fabrication process, we select aluminum (Al) as the coating material for all real-world prototypes. Fresnel coefficients for all materials are sourced from [Polyanskiy 2024].

Capture. We evaluate the fabricated reflectance by illuminating the wafer with a high-power white light source, focused to a 1 mm diameter spot. The light is incident at approximately 10°, ensuring minimal masking or self-shadowing. The reflected light is projected onto a diffuse white screen, where the angular reflectance pattern is recorded using a machine vision camera (FLIR Grasshopper 3, 5MP) at a viewing angle of ∼45 degrees.

To ensure accurate spatial and spectral comparison with the simulated BRDF, we apply geometric alignment and cropping to the captured image manually. We also perform white-balance calibration by imaging the same screen under identical illumination without the wafer and computing the average RGB intensity.

6 RESULTS

We evaluate our method across a diverse set of BRDFs, each optimized using the Adam optimizer with a momentum of 0.9 and a

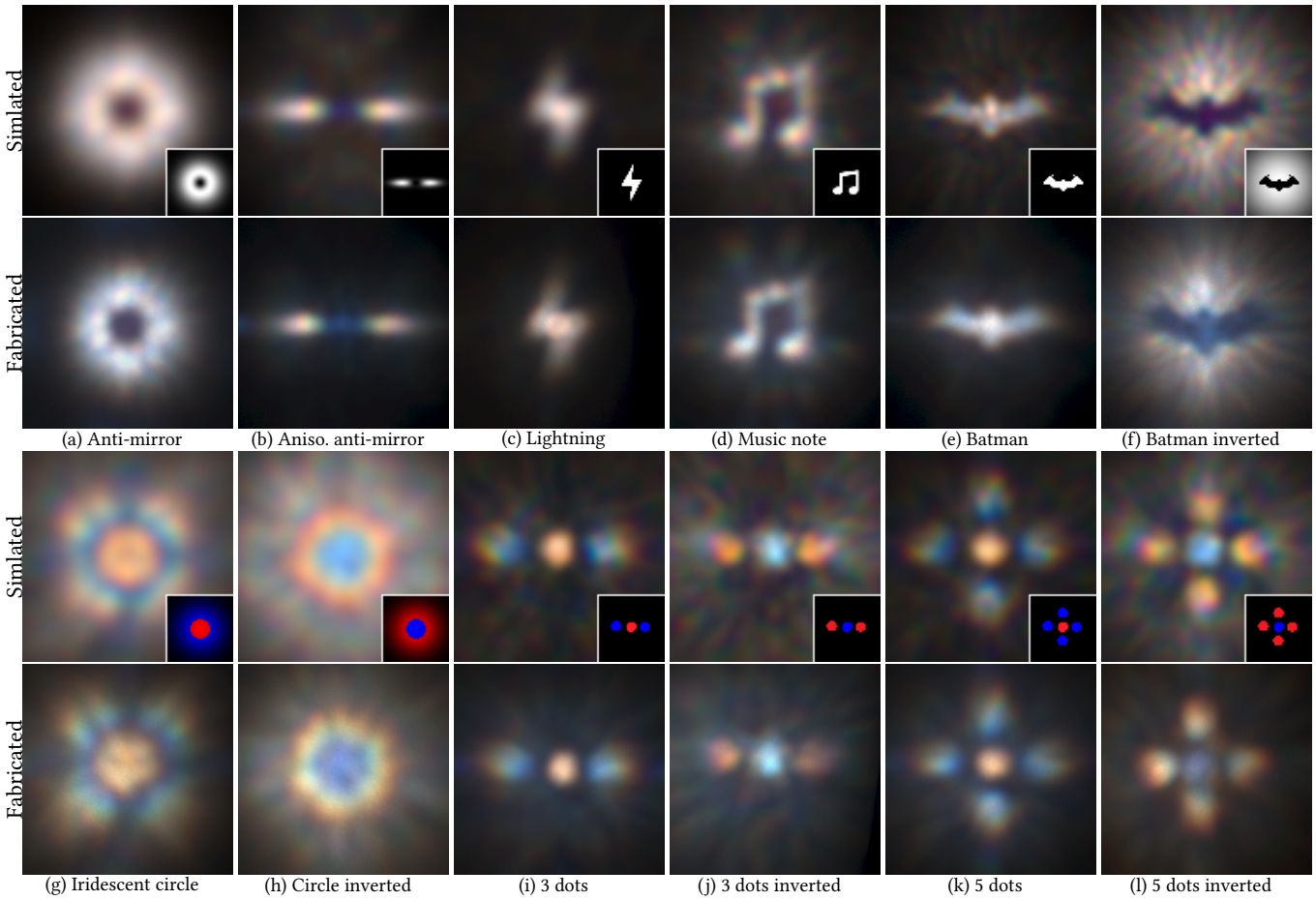

Fig. 11. Comparison between simulated and real fabricated BRDFs across different BRDF families. The first row shows the simulated results, with the target BRDF pattern shown in the inset. The second row displays the corresponding fabricated results captured under a controlled white-light setup. Each column presents one example from the following BRDF categories: (a)–(b) anti-mirrors, (c)–(f) pictorial reflections, and (g)–(i) various patterns of iridescent reflection. The results demonstrate that our method accurately translates simulated BRDFs into physical surfaces with complex angular and spectral behavior.

learning rate of 1×10^{-5}. All experiments are performed on a high-performance server equipped with dual AMD EPYC 7763 CPUs (768 GB DDR4 RAM) and a single NVIDIA GeForce RTX 4090 GPU. For a typical BRDF, convergence requires approximately 6–12 hours, depending on feature size and coherence area.

We organize our results into four representative BRDF families: (a) *anti-mirrors*, which suppress reflectance in the mirror direction [Levin et al. 2013], (b) *pictorial reflections*, which encode arbitrary spatial reflectance structures [Weyrich et al. 2009], (c) *structural colors*, which produce uniform colors visible within a certain angular range, and (d) *iridescences*, which generate view-dependent color shifts driven by diffraction. Figure 11 compares simulated BRDFs with real fabricated results across twelve examples. These results confirm that our end-to-end differentiable pipeline can generate complex angular and spectral reflectance profiles that are physically reproducible using grayscale lithography. Refer to the supplemental video for more results.

To evaluate and visualize BRDFs throughout our experiments, we visualize the outgoing 2D BRDF slice on the projected hemisphere as shown in Figure 13, illustrating how view directions along vertical and horizontal planes map directly to vertical and horizontal slices in the BRDF visualization. In this visualization, each pixel corresponds to a specific view direction, with the x- and y-axes of the image representing the x- and y-components of the viewing angle, respectively. The illumination direction is fixed to the surface normal $\mathbf{n}$, and reflectance is sampled across a hemisphere of view directions centered around the normal. The angular sampling range is defined as $[-\varphi, \varphi]$ in both axes, where φ denotes the maximum viewing angle.

Although we present these four categories for clarity and systematic comparison, our method is not constrained to any predefined BRDF type. Because our pipeline is fully differentiable and end-to-end, it can theoretically optimize toward any physically realizable BRDF pattern–bounded only by the coherence area, wavelength-dependent interference, and fabrication limits. Additional results, ablations, and parameters are provided in the supplemental material.

The fabricated wafers were produced using feature sizes of either 1.5 μm or 2.0 μm, with surface heights constrained to a maximum of 0.8 μm. To account for real-world fabrication artifacts, we simulate

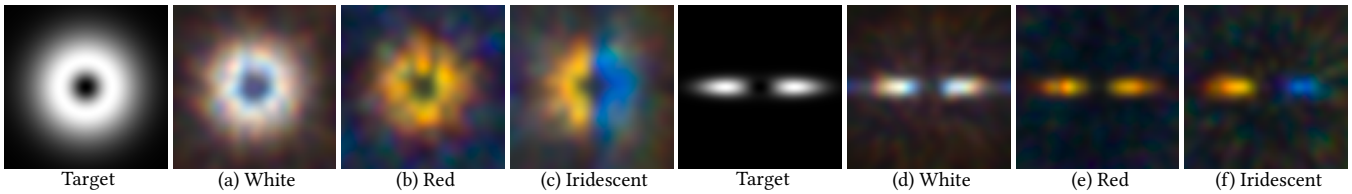

Fig. 12. Controlled color variants of anti-mirror BRDFs. We render isotropic and anisotropic anti-mirror designs simulated in white, red, and iridescent color schemes. The pipeline reproduces angular nulls and controllable chromaticity through phase-guided optimization.

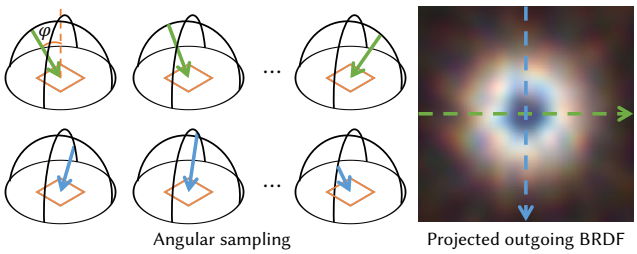

Fig. 13. We visualize outgoing BRDFs as projected images, where the x- and y-axes correspond to the x- and y-components of the view direction.

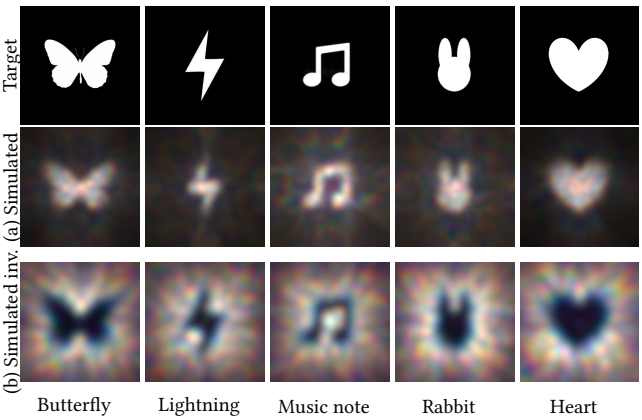

Fig. 14. Pictorial BRDFs encoding various icon shapes. We optimize height maps to match target reflectance patterns for six icons: Butterfly, Lightning, Music note, Rabbit, and Heart. Both original (row 2) and inverted (row 3) silhouettes are accurately rendered in angular reflectance. These results highlight our method's capability to generate arbitrary symbolic patterns.

the effects of optical blurring and process noise by applying a Gaussian smoothing kernel with standard deviation $\sigma_b = 0.65\,\mu$m estimated from microscopic surface measurements, and adding relative Gaussian noise with $\sigma_n = 0.075$ during training. Gamma correction ($\gamma = 2.2$) is also applied during both training and rendering to match human visual perception and camera response.

Unless otherwise specified, all training parameters are defined per-BRDF in Supplementary Table 2 in the supplemental document. In the following sections, we analyze the results of each BRDF family in detail and present ablation studies on fabrication noise, feature size, and other key factors that influence color quality. Also, additional ablations can be found in Supplementary Section F.

6.1 Anti-Mirror BRDFs

Anti-mirror BRDFs suppress reflectance in the mirror direction, creating angular *nulls* in the specular lobe. Figures 11(a)–(b) compare simulated and real fabricated results for both the isotropic and anisotropic anti-mirror cases. In both examples, the fabricated reflectance patterns closely match the simulated designs, including the intended suppression along the central axis and the distribution of light into off-specular directions. These results validate our method's ability to shape BRDFs by manipulating wave interference effects across coherence areas.

To explore the appearance control of anti-mirror patterns, we simulate three color variants for both isotropic and anisotropic cases: white, red, and iridescent (Figure 12). The red variants show strong color concentration at off-mirror directions, while the iridescent designs produce clear view-dependent spectral separation. These examples demonstrate that our framework enables not just angular suppression but also controllable coloration through structural wave design.

6.2 Pictorial BRDFs

One of the strengths of our pipeline is its ability to optimize reflectance patterns that represent complex and recognizable graphical shapes. Figures 11(c)–(f) show the fabricated, pictorial BRDFs that encode various symbolic shapes—Lightning, Music note, Batman, and Inverted Batman logo–along with their simulated counterparts. The fabricated patterns preserve both the coarse structure and the fine angular layout of the intended designs. Although some high-frequency edge details are smoothed due to lithographic blurring, the target shapes remain clearly identifiable, validating our method's spatial expressiveness.

In addition to fabrication, we demonstrate the flexibility of our pipeline in simulation by producing a wider set of pictorial BRDFs, including Butterfly, Lightning, Music note, Rabbit, and Heart (Figure 14). We optimize both original and inverted versions of each pattern. Despite strong symmetry or fine features in some designs, our method produces consistent angular reflectance that captures the silhouette and orientation of each pictorial shape.

6.3 Structural Color BRDFs

Our method enables control over both angular intensity and perceived color, allowing us to synthesize BRDFs that exhibit a uniform hue within a certain angular range. To explore the full color gamut, we simulate BRDFs designed to produce red, orange, yellow, green, cyan, blue, and purple (Figure 15). These structural color patterns demonstrate our pipeline's ability to selectively shape the spectrum

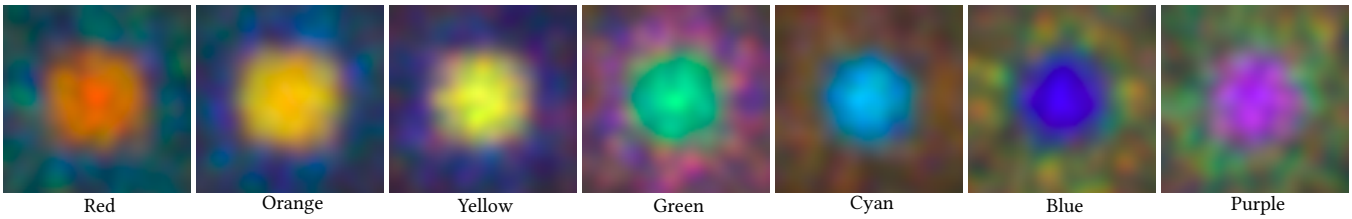

Fig. 15. Structural color BRDFs rendered across the visible spectrum. We optimize reflectance profiles to produce red, orange, yellow, green, cyan, blue, and purple hues with uniform intensity in a narrow angular range (~ 20°). By spatially mixing red, green, and blue BRDFs in micro-patch units, any RGB color can be approximated at the macro scale.

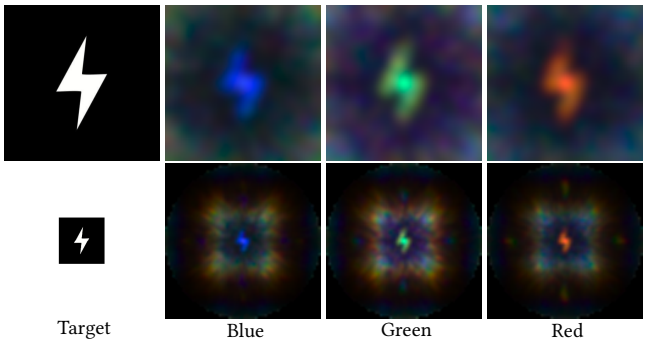

Fig. 16. Colored pictorial BRDFs using the Lightning pattern. We render pictorial BRDFs with dominant blue, green, and red spectral peaks. Top row shows angular reflectance within [-14°,14°], while bottom row visualizes wider angular views in [-90°, 90°], revealing that undesired colors are deflected outside the design's main lobe. This demonstrates angular spectral separation, enabling directional color control for graphical BRDFs.

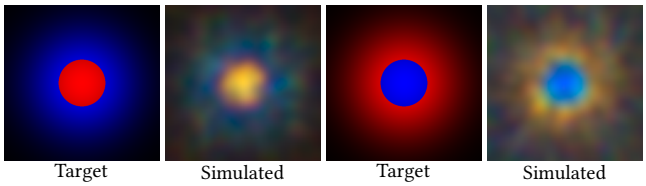

(a) Iridescent circle (b) Circle inverted

Fig. 17. Iridescent BRDFs for structured patterns. We render the color separation effects for diffuse patterns under wave-optical rendering with a feature size of 0.8 μm. Distinct view-dependent spectral shifts emerge due to directional interference, demonstrating programmable iridescence across angular space.

within a tight angular window (≈ 20°). By composing different patches (i.e., red, green, and blue) within small regions, we can linearly mix any RGB color at the macro scale, offering a fabrication-aware method for reflectance-based color design.

To further push the expressive capabilities of pictorial BRDFs, we incorporate spectral control to produce colored pictorial reflectance. In Figure 16, we use the Lightning symbol to demonstrate pictorial BRDFs rendered with dominant blue, green, and red colors. These reflectance profiles exhibit angular confinement of each color, showing that color-coded information can be encoded and separated based on viewing direction. The bottom row reveals that undesired spectral components are reflected into peripheral angles (outside the central design), confirming the angular selectivity enabled by our optimization.

6.4 Iridescent BRDFs

Beyond spatial and spectral control, our pipeline supports the design of iridescent BRDFs that exhibit view-dependent color shifts–produced purely through structural interference. Figures 11(g)–(l) show real fabricated BRDFs for circled, 3-dot, and 5-dot reflectance patterns, including their inverted counterparts. These examples exhibit vivid color separation across viewing directions, confirming the feasibility of encoding iridescent structure with micrometer-scale precision.

At larger viewing angles, the simulated BRDF in Figure 11(g) exhibits undesired red coloration, while Figure 11(h) reveals increased background noise and artifacts. These distortions arise from the limited control over angular reflectance when using relatively coarse feature sizes (2 μm). As shown in Figure 17, reducing the feature size significantly enhances angular precision and spectral fidelity in simulation. This trend suggests that further advancements in fabrication resolution could enable more accurate and cleaner reproduction of complex BRDFs, particularly those with strong directional and spectral constraints.

6.5 Ablation study

To evaluate the effect of feature resolution, we conduct an ablation study in both simulation and fabrication.

Figure 18 shows the impact of feature size on anti-mirror fidelity. We test two BRDFs (anisotropic anti-mirror with white color, and anti-mirror with iridescence) at three resolutions: 0.8 μm, 1.6 μm, and 2.4 μm. We observe that finer feature sizes enable more accurate angular pattern reproduction and preserve chromatic effects, especially in the iridescent case. In contrast, increasing the feature size leads to a noticeable loss of angular resolution and diminishes the structure's ability to modulate color through diffraction.

Consistently, fabricated results in Figure 19 reveal that BRDFs produced at 1.5 μm achieve higher color fidelity and sharper angular patterns than those fabricated at 2.0 μm. These trends confirm that feature size is a critical factor governing not only the spatial resolution of the reflectance but also the achievable angular spread and chromatic precision.

As shown in Figure 20, training with a larger smoothing kernel (over-smoothing) yields BRDFs that remain robust when rendered with the actual fabrication blur. In contrast, under-smoothing during training leads to noticeable artifacts and color distortion when tested under realistic conditions. These results suggest that, for structural color BRDFs in particular, it is preferable to conservatively overestimate the extent of fabrication blur in order to ensure

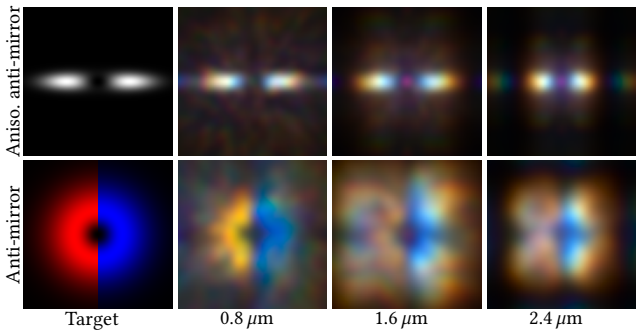

Fig. 18. Ablation study of feature size in anti-mirror BRDFs. We evaluate Anisotropic anti-mirror (white) and Anti-mirror (iridescent) across feature sizes of 0.8 μm, 1.6 μm, and 2.4 μm. Smaller features result in more precise angular control and enhanced color fidelity. Results demonstrate that smaller feature sizes (0.8 μm) significantly enhance the quality of both BRDFs. Conversely, larger feature sizes (2.4 μm) reduce the controllable angular range and eliminate color production capability.

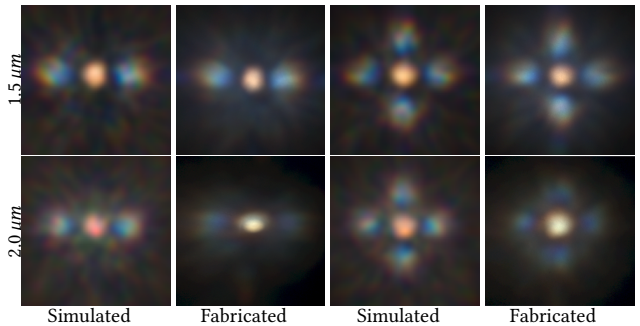

Fig. 19. Ablation study of the feature size for fabricated iridescent BRDFs. We optimize towards the same target–3 dots and 5 dots–using the feature sizes of 1.5 μm and 2.0 μm and fabricate the optimized heightmaps. Smaller features yield sharper angular definition and clearer chromatic separation, while larger features cause blur and reduce spectral resolution.

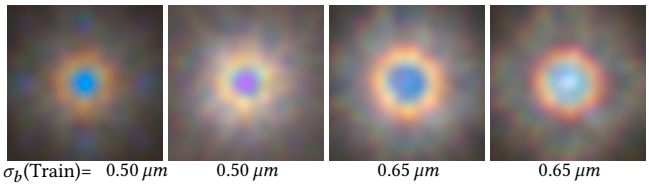

Fig. 20. Ablation study of training blur σ_b on the quality of Circle inverted. The first two columns show BRDFs optimized with $\sigma_b = 0.50\,\mu$m, while the last two use $\sigma_b = 0.65\,\mu$m during optimization. Each optimized height map is rendered under both smoothing levels ($\sigma_b = 0.50\,\mu$m and $0.65\,\mu$m) to test robustness. Under-smoothing during training leads to noticeable color shift and instability under blur. In contrast, over-smoothing results in a more stable appearance across rendering conditions. Note that Gaussian noise was excluded from both training and rendering to isolate the effect of smoothing.

stability and perceptual fidelity in the final appearance. For more additional ablation studies, please refer to Supplementary Section F in the supplemental document.

7 DISCUSSIONS

With higher fabrication precision, our method can realize a broader range of BRDFs with improved fidelity across both spatial and spectral dimensions. Simulated results for multiple BRDF families are presented in Figures 12, 14, 15, 16, and 17, covering anti-mirrors, pictorial reflections, structural colors, and iridescent patterns. The feature size, coherence area, blur kernel, and angular sampling parameters for each main BRDF result are listed in Supplementary Table 2.

Color. We observe that increasing the maximum height range sharpens the spectral peaks, bringing the curves closer to ideal RGB profiles (Figure 8). This introduces a trade-off: while taller structures improve spectral selectivity and color accuracy, they may also increase the risk of shadowing and masking. Similarly, reducing the BRDF intensity or using smaller feature sizes improves peak sharpness and chromatic contrast, but makes fabrication more challenging.

For Red and Blue BRDFs, some spectral energy lies outside the visible range. However, for Red, overlap with the green channel leads to a slight orange hue, while the Green spectrum lacks sufficient sharpness and mixes with adjacent blue and red wavelengths–reducing saturation. Refer to Supplemental Figure 9. These effects highlight the challenges of precisely targeting perceptual color with physical interference patterns.

Lastly, our small patch size enables spatial BRDF mixing at the macro scale. By tiling Red, Green, and Blue BRDF units within small regions, we can approximate arbitrary RGB colors through spatial averaging–similar in principle to subpixel layouts in displays. This opens opportunities for scalable, full-color reflectance patterning without requiring per-pixel spectral optimization.

Simulation vs. Fabrication. Despite strong visual agreement between simulated and fabricated BRDFs, we observe minor discrepancies in color and angular sharpness. These deviations stem from real-world factors not explicitly modeled during optimization, including surface scattering, inner refraction, and lithography-induced blurring. To isolate the effects of fabrication noise, we conduct a controlled ablation analysis in Figure 21. For the Anisotropic anti-mirror BRDF, we compare renderings of the same optimized height map using different Gaussian blur kernels. When rendered with a smaller blur ($\sigma_b = 0.50\,\mu$m) than used during training ($\sigma_b = 0.65\,\mu$m), the result shows increased blue reflection in the mirror direction–consistent with the dark blue fringe observed in the fabricated output. This suggests that underestimating fabrication blur during inference exaggerates unwanted angular reflections. Similarly, for the Circle inverted BRDF, adding relative Gaussian noise ($\sigma_n = 0.05$) to the optimized height map causes a noticeable shift in the central color from blue to purple, matching the appearance in the real captured result. These tests confirm that both angular and spectral discrepancies can be attributed to fabrication-related noise and structural deviations. While we incorporate noise modeling during training to improve robustness, the residual gap suggests that modeling alone is insufficient to fully compensate for real-world imperfections. Ultimately, improving fabrication precision would

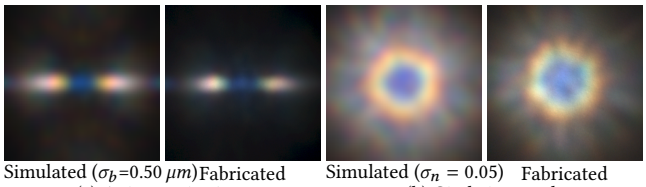

(a) Aniso. anti-mirror (b) Circle inverted

Fig. 21. Fabrication noise analysis using Anisotropic anti-mirror and Circle inverted BRDFs. Left: Anisotropic anti-mirror is optimized with σ_b = 0.65 μm blur, but rendered here with a smaller blur (σ_b = 0.50 μm), resulting in blue reflection along the mirror direction—consistent with the fabricated result. Right: Circle inverted is optimized normally, but adding relative Gaussian noise (σ_n = 0.05) during rendering shifts the central hue from blue to purple, closely matching the fabricated image. These results highlight how small deviations in fabrication blur or additive noise can explain observed discrepancies in spectral and angular behavior.

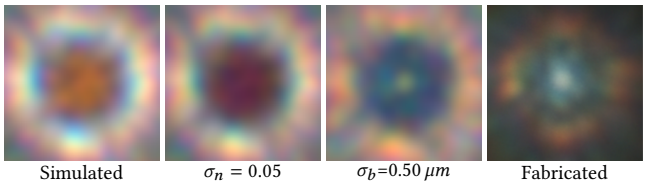

Fig. 22. Failure case from the color BRDF family illustrating extreme sensitivity to fabrication noise. Simulated results with added relative Gaussian noise (σ_n = 0.05) or reduced blur kernel (σ_b = 0.50 μm) show significant spectral distortion–especially in the red pattern. The fabricated result exhibits similar degradation, with desaturation and angular blur, confirming that structural color BRDFs–particularly red–are more vulnerable to process variation than other families.

significantly enhance the alignment between simulation and physical realization, particularly for BRDFs with high spectral or angular sensitivity.

Fabrication noise. Among the BRDF families we tested, structural color patterns–especially those with dominant red spectral components–exhibit the highest sensitivity to fabrication noise. Figure 22 presents a representative failure case where a red-encoded BRDF, fabricated with 1.5 μm feature size and realistic process noise, produces an unsatisfactory result. Compared to other BRDFs (e.g., Anti-mirror or Circle inverted in Figure 21), the same noise levels cause far more pronounced spectral distortion in the red pattern.

Specifically, adding relative Gaussian noise (σ_n = 0.05) or reducing the smoothing kernel size to σ_b = 0.5 μm causes the simulated red lobe to shift and desaturate—closely matching the real-fabricated image. This highlights that color BRDFs, particularly those relying on long-wavelength components, are more vulnerable to structural inaccuracies and require stricter fabrication tolerances.

Improving fabrication precision–either via reduced feature blur, better resist control, or higher-resolution lithography–could mitigate this sensitivity and enable fabrication of more saturated, rainbow-like BRDFs such as those demonstrated in simulation (e.g., Figure 15).

8 CONCLUSIONS

Our work introduces a differentiable wave-optics rendering pipeline for BRDF design, enabling joint optimization of surface geometry to control both the color and intensity of reflected light. This approach supports high-resolution surface modulation and is validated through real-world fabrication using grayscale lithography. Compared to previous methods, our framework can reproduce a significantly broader range of BRDFs, including anti-mirror, pictorial, colored, and iridescent patterns.

Nonetheless, several limitations remain. First, our model assumes a globally planar surface, and cannot yet be applied to curved or general 3D geometries. Second, the simulation ignores shadowing and masking effects, which can restrict the angular range and accuracy of reflectance in real-world conditions. Integrating more complete physical models–such as those in [Yu et al. 2023]–may mitigate this. Third, our fabrication method is constrained by the resolution and variability of grayscale lithography. The minimum feature size of 1.5 μm and fabrication-induced blur introduce spectral and spatial distortions, particularly for color BRDFs. Improved fabrication technologies, such as two-photon lithography, could enhance fidelity and unlock finer optical control.

This work represents an initial step toward fabricating full-color, directional reflectance on flat surfaces. Future directions include extending the pipeline to handle non-planar geometries, modeling the lithography process directly as part of the optimization loop, and incorporating advanced wave-optics frameworks (e.g., [Cuypers et al. 2012; Zhang and Levoy 2009]) to enable far-field diffraction and other light-field effects. These advances would allow for broader applications, from dynamic light encoding to fabrication-aware appearance design on arbitrary objects.

ACKNOWLEDGMENTS

Min H. Kim acknowledges the Samsung Research Funding & Incubation Center (SRFC-IT2402-02), the Korea NRF grant (RS-2024-00357548), the MSIT/IITP of Korea (RS-2022-00155620, RS-2024-00398830, 2022-0-00058, and 2017-0-00072), Microsoft Research Asia, and Samsung Electronics. Also, this work is partially supported by NSF China (62332015, 62227806 & 62421003) and the Information Technology Center and the State Key Lab of CAD&CG, Zhejiang University.

REFERENCES

Lubna Abu Rmaileh and Alan Brunton. 2023. Meso-Facets for Goniochromatic 3D Printing. *ACM Transactions on Graphics* 42 (07 2023), 1–12. https://doi.org/10.1145/3592137

Neil Gordon Alldrin and David J Kriegman. 2006. A planar light probe. In *2006 IEEE Computer Society Conference on Computer Vision and Pattern Recognition (CVPR'06)*, Vol. 2. IEEE, 2324–2330.

Jacob Andkjær, Villads Egede Johansen, Kasper Storgaard Friis, and Ole Sigmund. 2014. Inverse design of nanostructured surfaces for color effects. *J. Opt. Soc. Am. B* 31, 1 (Jan 2014), 164–174. https://doi.org/10.1364/JOSAB.31.000164

Sergio Lopera Aristizabal, Giuseppe A. Cirino, Arlindo N. Montagnoli, Aparecido Arruda Sobrinho, Jose Benaque Rubert, Michel Hospital, and Ronaldo D. Mansano. 2013. Microlens array fabricated by a low-cost grayscale lithography maskless system. *Optical Engineering* 52, 12 (2013), 125101. https://doi.org/10.1117/1.OE.52.12.125101

Michael Ashikmin, Simon Premože, and Peter Shirley. 2000. A microfacet-based BRDF generator. In *Proceedings of the 27th annual conference on Computer graphics and interactive techniques*. 65–74.

Thomas Auzinger, Wolfgang Heidrich, and Bernd Bickel. 2018. Computational design of nanostructural color for additive manufacturing. *ACM Transactions on Graphics (TOG)* 37, 4 (2018), 1–16.

Seung-Hwan Baek, Hayato Ikoma, Daniel S. Jeon, Yuqi Li, Wolfgang Heidrich, Gordon Wetzstein, and Min H. Kim. 2021. Single-shot Hyperspectral-Depth Imaging with Learned Diffractive Optics. In *Proc. IEEE International Conference on Computer Vision (ICCV) 2021.*

Petr Beckmann and Andre Spizzichino. 1987. The scattering of electromagnetic waves from rough surfaces. *Artech House* (1987).

Max Born and Emil Wolf. 1997. Principles of optics. sixth (corrected) edition.

Linyou Cao, Pengyu Fan, Edward Barnard, Ana Brown, and Mark Brongersma. 2010. Tuning the Color of Silicon Nanostructures. *Nano letters* 10 (07 2010), 2649–54. https://doi.org/10.1021/nl1013794

Praneeth Chakravarthula, Yifan Peng, Joel Kollin, Henry Fuchs, and Felix Heide. 2019. Wirtinger holography for near-eye displays. *ACM Transactions on Graphics (TOG)* 38, 6 (2019), 213.

Feiliang Chen, Shao-Wei Wang, Xingxing Liu, Ruonan Ji, Zhifeng Li, Xiaoshuang Chen, Yuwei Chen, and Wei Lu. 2016. Colorful solar selective absorber integrated with different colored units. *Opt. Express* 24, 2 (Jan 2016), A92–A103. https://doi.org/10.1364/OE.24.000A92

Ni Chen, Congli Wang, and Wolfgang Heidrich. 2023. $\partial\mathbf{H}$: Differentiable Holography. *Laser & Photonics Reviews* 17, 9 (2023), 2200828. https://doi.org/10.1002/lpor.202200828

Yu Chen, Yang Li, Wenhao Tang, Yutao Tang, Yue Hu, Zixian Hu, Junhong Deng, Kokwai Cheah, and Guixin Li. 2022. Centimeter scale color printing with grayscale lithography. *Advanced Photonics Nexus* 1, 2 (2022), 026002. https://doi.org/10.1117/1.APN.1.2.026002

Xavier Chermain, Cédric Zanni, Jonàs Martínez, Pierre-Alexandre Hugron, and Sylvain Lefebvre. 2023. Orientable dense cyclic infill for anisotropic appearance fabrication. *ACM Transactions on Graphics (TOG)* 42, 4 (2023), 1–13.

Kyungjae Chung, Sunkyu Yu, Chul-Joon Heo, Jae Shim, Seung-Man Yang, Moon Han, Hong-Seok Lee, Yongwan Jin, Sang Lee, Namkyoo Park, and Jung-Hyuk Shin. 2012. Angle-Independent Reflectors: Flexible, Angle-Independent, Structural Color Reflectors Inspired by Morpho Butterfly Wings (Adv. Mater. 18/2012). *Advanced materials (Deerfield Beach, Fla.)* 24 (05 2012), 2375–9. https://doi.org/10.1002/adma.201200521

Robert L Cook and Kenneth E. Torrance. 1982. A reflectance model for computer graphics. *ACM Transactions on Graphics (ToG)* 1, 1 (1982), 7–24.

Tom Cuypers, Tom Haber, Philippe Bekaert, Se Baek Oh, and Ramesh Raskar. 2012. Reflectance model for diffraction. *ACM Trans. Graph.* 31, 5, Article 122 (sep 2012), 11 pages. https://doi.org/10.1145/2231816.2231820

Qinyuan Deng, Yong Yang, Hongtao Gao, Yi Zhou, Yu He, and Song Hu. 2017. Fabrication of Micro-Optics Elements with Arbitrary Surface Profiles Based on One-Step Maskless Grayscale Lithography. *Micromachines* 8, 10 (2017). https://doi.org/10.3390/mi8100314

Daljit Singh Dhillon, Jeremie Teyssier, M. Single, Iaroslav Gaponenko, Michel Milinkovitch, and Matthias Zwicker. 2014. Interactive Diffraction from Biological Nanostructures. *Computer Graphics Forum* 33 (12 2014). https://doi.org/10.1111/cgf.12425

Roberto Fallica, Robert Kirchner, Helmut Schift, and Yasin Ekinci. 2017. High-resolution grayscale patterning using extreme ultraviolet interference lithography. *Microelectronic Engineering* 177 (2017), 1–5. https://doi.org/10.1016/j.mee.2017.01.007 Advances in Micro- and Nano-Patterning.

Viggo Falster, Adrian Jarabo, and Jeppe Revall Frisvad. 2020. Computing the bidirectional scattering of a microstructure using scalar diffraction theory and path tracing. In *Computer Graphics Forum*, Vol. 39. 231–242.

Alban Fichet, Romain Pacanowski, and Alexander Wilkie. 2021. An OpenEXR layout for spectral images. *Journal of Computer Graphics Techniques* (2021).

Daniel Franklin, Yuan Chen, Abraham Vazquez-Guardado, Sushrut Modak, Javaneh Boroumand Azad, Daming Xu, Shin-Tson Wu, and Debashis Chanda. 2015. Polarization-independent actively tunable colour generation on imprinted plasmonic surfaces. *Nature Communications* 6 (06 2015), 7337.

Joseph W. Goodman. 1968. *Introduction to Fourier optics.* McGrawHill Book Company.

Anya Grushina. 2019. Direct-write grayscale lithography. *Advanced Optical Technologies* 8, 3-4 (2019), 163–169. https://doi.org/doi:10.1515/aot-2019-0024

Jun Han, Dong-Young Kim, Dohong Kim, and Kyung Choi. 2016. Highly conductive and flexible color filter electrode using multilayer film structure. *Scientific Reports* 6 (07 2016), 29341. https://doi.org/10.1038/srep29341

James E. Harvey. 1977. Light-Scattering Characteristics Of Optical Surfaces. In *Stray Light Problems in Optical Systems*, John D. Lytle and Howard E. Morrow (Eds.), Vol. 0107. International Society for Optics and Photonics, SPIE, 41 – 47. https://doi.org/10.1117/12.964594

Nicolas Holzschuch and Romain Pacanowski. 2017. A two-scale microfacet reflectance model combining reflection and diffraction. *ACM Trans. Graph.* 36, 4, Article 66 (jul 2017), 12 pages. https://doi.org/10.1145/3072959.3073621

Matthias B. Hullin, Hendrik P. A. Lensch, Ramesh Raskar, Hans Peter Seidel, and Ivo Ihrke. 2011. Dynamic Display of BRDFs. *Computer Graphics Forum* 30, 2 (2011), 475–483.

Victoria Hwang, Anna B. Stephenson, Solomon Barkley, Soeren Brandt, Ming Xiao, Joanna Aizenberg, and Vinothan N. Manoharan. 2021. Designing angle-independent structural colors using Monte Carlo simulations of multiple scattering. *Proceedings of the National Academy of Sciences* 118, 4 (2021), e2015551118. https://doi.org/10.1073/pnas.2015551118 arXiv:https://www.pnas.org/doi/pdf/10.1073/pnas.2015551118

Daniel S. Jeon, Seung-Hwan Baek, Shinyoung Yi, Qiang Fu, Xiong Dun, Wolfgang Heidrich, and Min H. Kim. 2019. Compact Snapshot Hyperspectral Imaging with Diffracted Rotation. *ACM Transactions on Graphics (Proc. SIGGRAPH 2019)* 38, 4 (2019), 117:1–13.

Villads Egede Johansen, Jacob Andkjær, and Ole Sigmund. 2014. Design of structurally colored surfaces based on scalar diffraction theory. *J. Opt. Soc. Am. B* 31, 2 (Feb 2014), 207–217. https://doi.org/10.1364/JOSAB.31.000207

Villads Egede Johansen, Lasse Højlund Thamdrup, Kristian Smistrup, Theodor Nielsen, Ole Sigmund, and Peter Vukusic. 2015. Designing visual appearance using a structured surface. *Optica* 2, 3 (Mar 2015), 239–245. https://doi.org/10.1364/OPTICA.2.000239

Micah K Johnson, Forrester Cole, Alvin Raj, and Edward H Adelson. 2011. Microgeometry capture using an elastomeric sensor. *ACM Transactions on Graphics (TOG)* 30, 4 (2011), 1–8.

Bernhard Kerbl, Georgios Kopanas, Thomas Leimkühler, and George Drettakis. 2023. 3D Gaussian Splatting for Real-Time Radiance Field Rendering. *ACM Transactions on Graphics* 42, 4 (July 2023). https://repo-sam.inria.fr/fungraph/3d-gaussian-splatting/

Anat Levin, Daniel Glasner, Ying Xiong, Frédo Durand, William Freeman, Wojciech Matusik, and Todd Zickler. 2013. Fabricating BRDFs at high spatial resolution using wave optics. *ACM Trans. Graph.* 32, 4, Article 144 (jul 2013), 14 pages. https://doi.org/10.1145/2461912.2461981

Joakim Löw, Joel Kronander, Anders Ynnerman, and Jonas Unger. 2012. BRDF models for accurate and efficient rendering of glossy surfaces. *ACM Trans. Graph.* 31, 1, Article 9 (feb 2012), 14 pages. https://doi.org/10.1145/2077341.2077350

Andrea Luongo, Viggo Falster, Mads Brix Doest, Macarena Mendez Ribo, Eyþór Rúnar Eiríksson, David B Pedersen, and Jeppe Revall Frisvad. 2020. Microstructure control in 3D printing with digital light processing. In *Computer Graphics Forum*, Vol. 39. Wiley Online Library, 347–359.

M. Mühlberger, M. Rohn, J. Danzberger, E. Sonntag, A. Rank, L. Schumm, R. Kirchner, C. Forsich, S. Gorb, B. Einwögerer, E. Trappl, D. Heim, H. Schift, and I. Bergmair. 2015. UV-NIL fabricated bio-inspired inlays for injection molding to influence the friction behavior of ceramic surfaces. *Microelectronic Engineering* 141 (2015), 140–144. https://doi.org/10.1016/j.mee.2015.02.051 Micro/Nano Fabrication 2014.

Yifan Peng, Qiang Fu, Felix Heide, and Wolfgang Heidrich. 2016. The diffractive achromat full spectrum computational imaging with diffractive optics. In *SIGGRAPH ASIA 2016 Virtual Reality meets Physical Reality: Modelling and Simulating Virtual Humans and Environments*. 1–2.

Yifan Peng, Qilin Sun, Xiong Dun, Gordon Wetzstein, Wolfgang Heidrich, and Felix Heide. 2019. Learned large field-of-view imaging with thin-plate optics. *ACM Trans. Graph.* 38, 6, Article 219 (Nov. 2019), 14 pages. https://doi.org/10.1145/3355089.3356526

Thiago Pereira, Carolina LA Paes Leme, Steve Marschner, and Szymon Rusinkiewicz. 2017. Printing anisotropic appearance with magnetic flakes. *ACM Transactions on Graphics (TOG)* 36, 4 (2017), 1–10.

Maxine Perroni-Scharf and Szymon Rusinkiewicz. 2023. Constructing Printable Surfaces with View-Dependent Appearance. In *ACM SIGGRAPH 2023 Conference Proceedings* (Los Angeles, CA, USA) *(SIGGRAPH '23)*. Association for Computing Machinery, New York, NY, USA, Article 51, 10 pages. https://doi.org/10.1145/3588432.3591526

Michal Piovarci, Michael Foshey, Vahid Babaei, Szymon Rusinkiewicz, Wojciech Matusik, and Piotr Didyk. 2020. Towards spatially varying gloss reproduction for 3D printing. *ACM Trans. Graph.* 39, 6, Article 206 (Nov. 2020), 13 pages.

Mikhail N Polyanskiy. 2024. Refractiveindex. info database of optical constants. *Scientific Data* 11, 1 (2024), 94.

Peiran Ren, Jiaping Wang, John Snyder, Xin Tong, and Baining Guo. 2011. Pocket reflectometry. *ACM Transactions on Graphics (TOG)* 30, 4 (2011), 1–10.

Kaisei Sakurai, Yoshinori Dobashi, Kei Iwasaki, and Tomoyuki Nishita. 2018. Fabricating reflectors for displaying multiple images. *ACM Transactions on Graphics (TOG)* 37, 4 (2018), 1–10.

Pengfei Shen, Ruizeng Li, Beibei Wang, and Ligang Liu. 2023. Scratch-based Reflection Art via Differentiable Rendering. *ACM Trans. Graph.* 42, 4, Article 65 (July 2023), 12 pages. https://doi.org/10.1145/3592142

Yichen Shen, Veronika Rinnerbauer, Imbert Wang, Veronika Stelmakh, John Joannopoulos, and Marin Soljacic. 2014. Structural Colors from Fano Resonances. *ACS Photonics* 2 (12 2014), 27–32. https://doi.org/10.1021/ph500400w

Zheng Shi, Ilya Chugunov, Mario Bijelic, Geoffroi Côté, Jiwoon Yeom, Qiang Fu, Hadi Amata, Wolfgang Heidrich, and Felix Heide. 2024. Split-aperture 2-in-1 computational cameras. *ACM Transactions on Graphics (TOG)* 43, 4 (2024), 1–19.

Vincent Sitzmann, Steven Diamond, Yifan Peng, Xiong Dun, Stephen Boyd, Wolfgang Heidrich, Felix Heide, and Gordon Wetzstein. 2018. End-to-end optimization of optics and image processing for achromatic extended depth of field and super-resolution imaging. *ACM Trans. Graph.* 37, 4, Article 114 (July 2018), 13 pages. https://doi.org/10.1145/3197517.3201333

Jos Stam. 1999. Diffraction shaders. In *Proceedings of the 26th Annual Conference on Computer Graphics and Interactive Techniques (SIGGRAPH '99)*. ACM Press/Addison-Wesley Publishing Co., USA, 101–110. https://doi.org/10.1145/311535.311546

Qilin Sun, Ethan Tseng, Qiang Fu, Wolfgang Heidrich, and Felix Heide. 2020. Learning Rank-1 Diffractive Optics for Single-Shot High Dynamic Range Imaging. In *Proceedings of the IEEE/CVF Conference on Computer Vision and Pattern Recognition (CVPR)*.

Zdravko Velinov, S. Werner, and Matthias Hullin. 2018. Real-Time Rendering of Wave-Optical Effects on Scratched Surfaces. *Computer Graphics Forum* 37 (05 2018), 123–134. https://doi.org/10.1111/cgf.13347

Yasi Wang, Mengjie Zheng, Qifeng Ruan, Yanming Zhou, Yiqin Chen, Peng Dai, Zheng-Mei Yang, Zihao Lin, Yuxiang Long, Ying Li, Na Liu, Cheng-Wei Qiu, and Joel Yang. 2018. Stepwise-Nanocavity-Assisted Transmissive Color Filter Array Microprints. *Research* 2018 (09 2018), 1–10. https://doi.org/10.1155/2018/8109054

Sebastian Werner, Zdravko Velinov, Wenzel Jakob, and Matthias B. Hullin. 2017. Scratch iridescence: wave-optical rendering of diffractive surface structure. *ACM Trans. Graph.* 36, 6, Article 207 (nov 2017), 14 pages. https://doi.org/10.1145/3130800.3130840

Tim Weyrich, Pieter Peers, Wojciech Matusik, and Szymon Rusinkiewicz. 2009. Fabricating microgeometry for custom surface reflectance. *ACM Transactions on Graphics (TOG)* 28, 3 (2009), 1–6.

Hongzhi Wu, Julie Dorsey, and Holly Rushmeier. 2011. Physically-based interactive bi-scale material design. *ACM Transactions on Graphics (TOG)* 30, 6 (2011), 1–10.

Skylar Wurster, Ran Zhang, and Changxi Zheng. 2024. Gabor Splatting for High-Quality Gigapixel Image Representations. In *ACM SIGGRAPH 2024 Posters* (Denver, CO, USA) *(SIGGRAPH '24)*. Association for Computing Machinery, New York, NY, USA, Article 66, 2 pages. https://doi.org/10.1145/3641234.3671081

Zhiyi Xuan, Junyu Li, Qingquan Liu, Fei Yi, Shaowei Wang, and Wei Lu. 2021. Artificial structural colors and applications. *The Innovation* 2, 1 (2021).

Ling-Qi Yan, Milos Hasan, Bruce Walter, Steve Marschner, and Ravi Ramamoorthi. 2018. Rendering specular microgeometry with wave optics. *ACM Trans. Graph.* 37, 4, Article 75 (jul 2018), 10 pages. https://doi.org/10.1145/3197517.3201351

Yunchen Yu, Mengqi Xia, Bruce Walter, Eric Michielssen, and Steve Marschner. 2023. A Full-Wave Reference Simulator for Computing Surface Reflectance. *ACM Trans. Graph.* 42, 4, Article 109 (jul 2023), 17 pages. https://doi.org/10.1145/3592414

Zhengyun Zhang and Marc Levoy. 2009. Wigner distributions and how they relate to the light field. In *2009 IEEE International Conference on Computational Photography (ICCP)*. 1–10. https://doi.org/10.1109/ICCPHOT.2009.5559007

Xiaolong Zhu, Christoph Vannahme, Emil Hojlund-Nielsen, N. Mortensen, and Anders Kristensen. 2015. Plasmonic colour laser printing. *Nature Nanotechnology* 11 (12 2015).

Gordon Zyla, Alexander Kovalev, Cemal Esen, Andreas Ostendorf, and Stanislav Gorb. 2022. Two-photon polymerization as a potential manufacturing tool for biomimetic engineering of complex structures found in nature. *Journal of Optical Microsystems* 2, 3 (2022), 031203–031203.